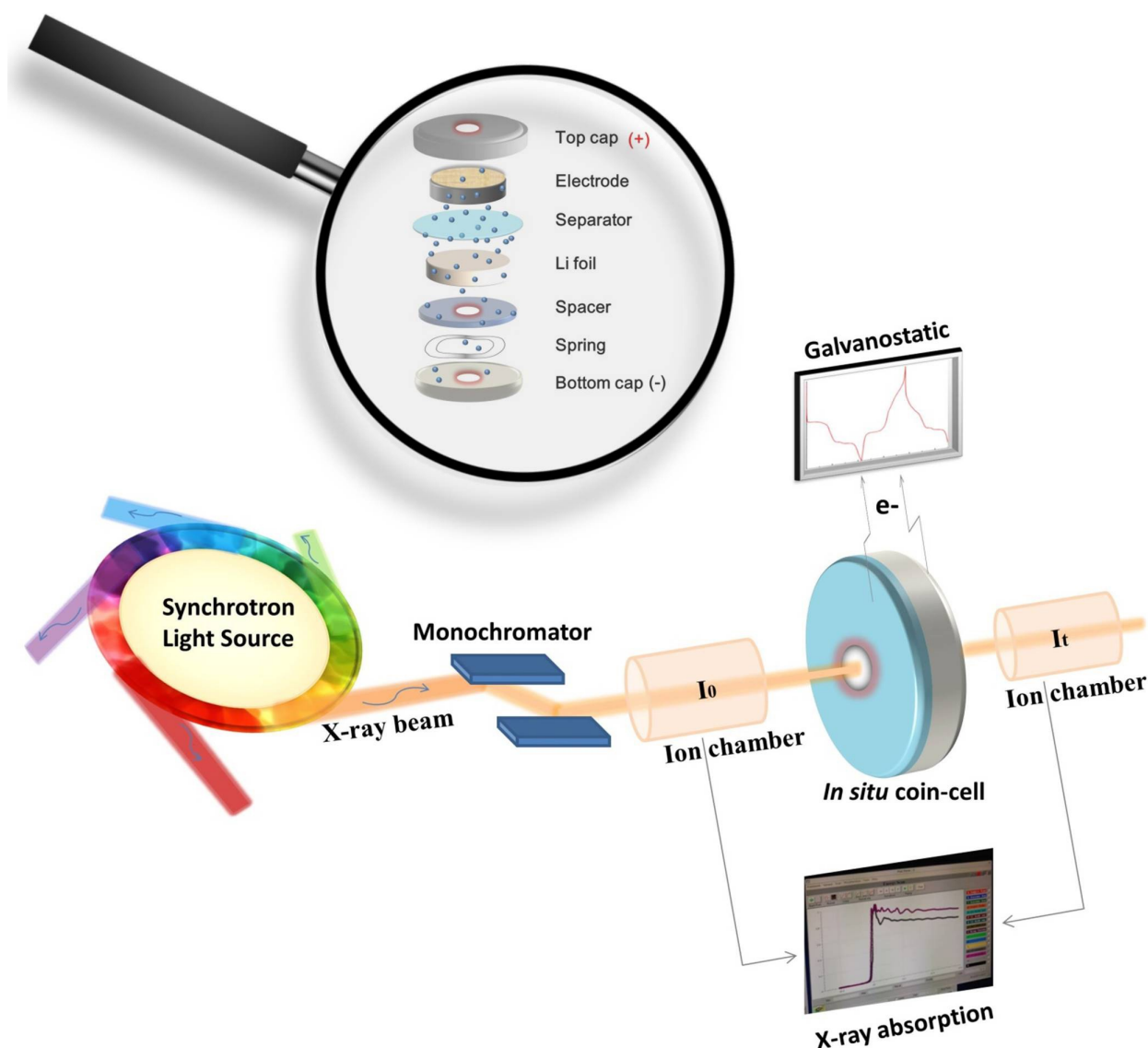Check for updates

Special Collection

In Situ Synchrotron X-Ray Absorption Spectroscopy Studies of Anode Materials for Rechargeable Batteries

Zhibin Wu,[a, c] Wei Kong Pang,[a] Libao Chen,*[c] Bernt Johannessen,*[b] and Zaiping Guo*[a]

Taking advantage of a high-flux light source, synchrotron X-ray absorption spectroscopy (XAS) beamline is able to perform *in situ/ex situ*, element-selective, and qualitative/quantitative experiments to elucidate electrochemical reaction mechanisms of batteries accurately and efficiently. *In situ* synchrotron XAS probes dynamic electronic and local atomic structure information, including valence state, charge transfer, local geometry and symmetry, bond number/length/type and disorder degree, of target elements of significance during battery operation, which facilitates to promote the development of rechargeable batteries by building accurate structure-performance relationships fundamentally. In this review, the basic principles for XAS are briefly introduced, design strategies for *in situ* XAS experiments are proposed, salient *in situ* XAS studies of battery anodes are summarized, and current challenges and future opportunities based on XAS measurements are also outlined.

1. Introduction

Electrochemical energy storage technologies play an important role in alleviating environmental pollution and the depletion of non-renewable resources. The increasing demands arising from electric vehicles, portable electronic devices, and stationary applications (e.g., home solar-power storage and smart power grids) pose a great challenge toward designing high-performance energy storage/conversion devices.[1] At present, lithium-ion batteries (LIBs) have wide commercial applications in consumer electronics, but their further applications in large-scale and high-rate energy storage applications, such as in electric vehicles and smart power grids, are suppressed by the rarity and high price of lithium resources, and the poor rate capability of graphite anodes.[2] A shift towards low-cost alternative storage systems, such as sodium-ion batteries (SIBs) and potassium-ion batteries (PIBs), is expected, whilst promising alternative anodes that have better rate capability, larger theoretical capacity and higher safety are also urgently needed.[3]

A typical Li-ion battery stores electric power as chemical energy reversibly between two electrodes (the anode and the cathode) which are separated by a polymer separator immersed in a liquid electrolyte (Figure 1a). The electrolyte transports ionic components through an ion-conductive but electron-insulative polymer separator inside the cell and forces the electrons to traverse an external circuit.[4] Upon charge, being forced by an applied voltage, lithium ions are extracted from cathode materials, followed by diffusing/migrating via the electrolyte, and then intercalate into anode materials. Upon discharge, the diffusing/migrating directions are reversed, along with the release of the output power (electrons flowing) to an external circuit.[4b,5] Interestingly, SIBs and PIBs share the same "rocking chair" operating principle as their Li-ion counterparts.[6] Promising alternative anodes, including Sn,[7] Sb,[8] Si,[9] SnO_2,[10] Nb_2O_5,[11] etc., have been widely investigated for rechargeable batteries, due to their higher capacity and/or better rate capability than the current commercial anode materials, i.e. graphite. Regarding the reaction mechanisms of electrode materials, anode materials can be classified into three classic types, that is insertion-, alloying-, and conversion-type anodes (Figure 1b).[5,12] As is well known, rechargeable batteries are extremely complex systems, involving solid/liquid/gas states, crystalline/amorphous phases, and structural/volumetric changes during cycling.[13] However, fundamental sciences relating to battery operation still lack of comprehensive and insightful understanding, including phase transformation mechanisms, interface interactions, electrode degradation, electrolyte decomposition, and components/evolutions of solid electrolyte interphase.[14] Recently, there are growing interests in developing advanced *in situ* characterization methods, such as synchrotron X-ray diffraction (XRD) and transmission electron microscopy (TEM), to characterize crystalline phase transformations and volumetric changes, which promote the fundamental understanding of battery mechanisms. However, XRD, for instance, is not able to analyze amorphous and poor crystalline phases whilst TEM may exert electron radiation damage to specimens and has rigid requirement for preparing specimens.[15] There are still significant challenges toward understanding the electrochemical reaction processes and failure mechanisms of anode materials for rechargeable batteries by using *in situ* techniques. Developing other state-of-the-art *in situ* techniques that deepen the understanding of the structure-performance relationship is of critical importance for rechargeable batteries.

Synchrotron X-ray absorption spectroscopy (XAS), a local structure probe technique, can detect all states of matter, including both amorphous and crystalline matter in solid or liquid forms, which facilitates an in-depth study on a large variety of electrode materials.[16] More important is that it can provide an *in situ* probe of dynamic charge transfer, redox reaction evolution, and changes in the local coordination environment of a selected element in the electrode during battery operation.[17] In this way, XAS can provide a unique view of the electrochemical reaction mechanisms for recharge-

[a] Dr. Z. Wu, Dr. W. Kong Pang, Prof. Z. Guo
Institute for Superconducting & Electronic Materials
School of Mechanical, Materials,
Mechatronic and Biomedical Engineering
University of Wollongong
Wollongong, NSW 2522, Australia
E-mail: zguo@uow.edu.au

[b] Dr. B. Johannessen
Australian Synchrotron
ANSTO
800 Blackburn Rd, Clayton, VIC 3168, Australia
E-mail: berntj@ansto.gov.au

[c] Dr. Z. Wu, Prof. L. Chen
State Key Laboratory for Powder Metallurgy
Central South University
Changsha, 410083, China
E-mail: lbchen@csu.edu.cn

[Special Collection] An invited contribution to a joint Special Collection between Batteries & Supercaps and Chemistry-Methods on In Situ and Operando Methods for Energy Storage and Conversion

able batteries beyond XRD,[15a] neutron powder diffraction,[18] TEM[15b] and so on, which would, in turn, inform more sensible battery design strategies.

Given that XAS analyses of cathode materials have recently been summarized in several reviews[15a,19] and there is no up-to-date review about XAS analyses of battery anodes, it is time to review the progress of XAS analyses of anode materials, which facilitates to promote the development of battery anodes and give a useful XAS tutorial for battery researchers. In this review, we will focus exclusively on *in situ* XAS studies of battery anodes. XAS-related basic principles, experimental design strategies, research advances and future development will be summarized and discussed.

2. X-Ray Absorption Spectroscopy (XAS) Fundamentals and Measurements

2.1. Principles of XAS

XAS, also referred to as X-ray absorption fine structure (XAFS), is a synchrotron-based technique that measures the X-ray absorption coefficient μ as a function of photon energy E near and above the threshold of the absorption edge of a selected element.[17a] An XAS spectrum is collected by tuning the photon energy, using a crystal or plane grating monochromator, to a specific range where core electrons can be excited. According to the measuring range of photon energies, XAS beamlines at synchrotron facilities worldwide can be typically classified into two types, namely soft XAS Beamlines (0.1–3 keV) and hard XAS Beamlines (above 4 keV).[20] Soft XAS beamlines are well suited to measure low atomic number (low-Z) elements such as C and O at the K-edge (viz. absorptions with an initial state of $n=1$), and high-Z elements through the alphabet (e.g., excitations from $n=2$ are termed L-edge, etc.), but it is only capable of probing surfaces and near-surface interfacial layers (from several nanometer to hundreds of nanometers) due to the shallow penetration depth of soft X-rays. Soft XAS spectra can be tested both in an electron yield mode (with the total electron yield mode probing a depth of ~10 nm and the partial electron yield probing a depth of ~5 nm determined by the electron mean-free path) and a fluorescence yield mode (probing a "bulk" depth of ~100 nm determined by the photon mean-free path).[21] Hard XAS beamlines with high penetration are advantageous to measure high-Z elements (such as transition metals) at the K-edge or L-edges in transmission mode, probing bulk depths in the microns and millimeters ranges, which allows *in situ* XAS experiments to be conducted conveniently *during* battery operation.[22] Hard XAS experiments
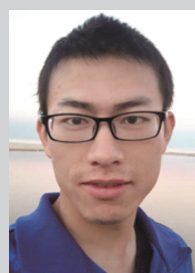
Zhibin Wu received his B. S. degree and M. S. degree from Central South University, China. Then, he obtained his Ph.D. degree in 2021 from the University of Wollongong, Australia, where he was supervised by Prof. Zaiping Guo and Dr. Bernt Johannessen. His current interests mainly focus on investigating the mechanism and performance of alkali metal-ion batteries, and the synchrotron techniques relating to X-ray absorption spectroscopy and powder diffraction.

Wei Kong Pang is currently a senior research fellow of Institute for Superconducting and Electronic Materials (ISEM), University of Wollongong, Australia, and an Australian Research Council (ARC) Future Fellow. His expertise includes the characterization of the atomic-level structure and dynamics of electrode materials for lithium-, sodium-, and potassium-ion batteries, via constructing the structure-function relations and pioneering the in operando methodologies using neutron and synchrotron X-ray techniques.

Libao Chen is a professor in the State Key Laboratory for Power Metallurgy at the Central South University, China. He received his Ph.D. degree in Materials Physics and Chemistry from the Shanghai Institute of Microsystem and Information Technology, Chinese Academy of Sciences in 2007. His research focuses on high performance electrode materials and electrochemical energy storage systems, including Li-ion batteries, Na-ion batteries and supercapacitors.

Bernt Johannessen is a Senior Beamline Scientist at the XAS Beamline at the Australian Synchrotron, Melbourne. He obtained a B.Sc. from the University of Auckland, New Zealand, and a Ph.D. from the Australian National University, Australia. He has about 20 years' experience with X-ray Absorption Spectroscopy including positions at the Australian Synchrotron and Photon Factory, Japan. Areas of scientific interests include energy storage and catalysis.

Zaiping Guo is a distinguished professor and an Australian Research Council (ARC) Future Fellow (FT3) at the Institute for Superconducting and Electronic Materials (ISEM), School of Mechanical, Materials, Mechatronic, and Biomedical Engineering, University of Wollongong, Australia. She received her Ph.D. degree from the University of Wollongong in 2003. Her current research interest mainly focuses on the energy storage such as lithium-ion batteries, sodium-ion batteries, potassium-ion batteries and hydrogen storage, as well as electrochemistry characterization and computer modelling.
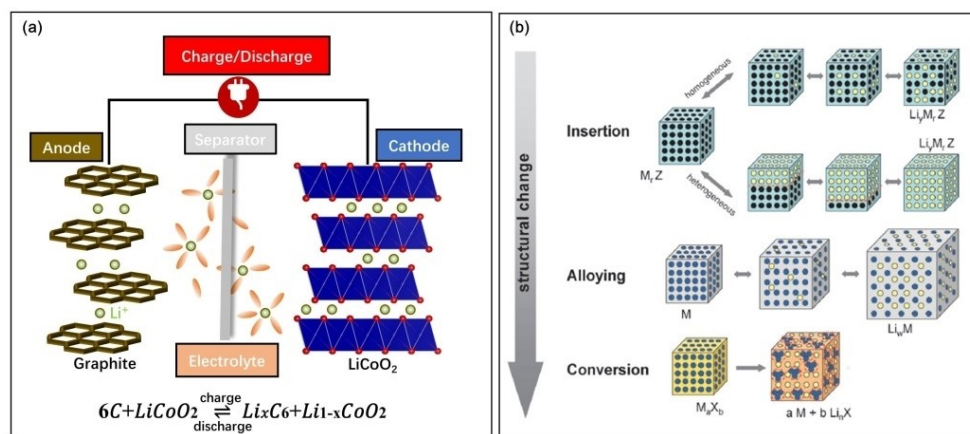
Figure 1. a) Schematic illustrations of a typical graphite/LiCoO₂ cell. b) Schematic illustrations of different reaction mechanisms of electrode materials for LIB anodes. Black, blue and yellow circles represent vacant sites, metal, and lithium-ions, respectively. Reproduced from Ref. [12] with permission. Copyright (2009) Royal Society of Chemistry.

can also be performed as a more surface-sensitive technique in fluorescence mode. Given that hard X-rays can be used at ambient conditions and can penetrate materials consisting of light elements easily (such as separators, electrolytes and covered windows) while soft X-rays typically require a vacuum setup and probes a shallow depth, hard XAS analysis will be of

focus in the following discussions about *in situ* XAS studies of batteries.

As shown in Figure 2a and b, when a target sample is bombarded with synchrotron X-rays of specific energy in an X-ray absorption experiment, some X-rays are absorbed by the atoms in the sample, leading to the excitation or ejection of core electrons physically into unoccupied electronic states or
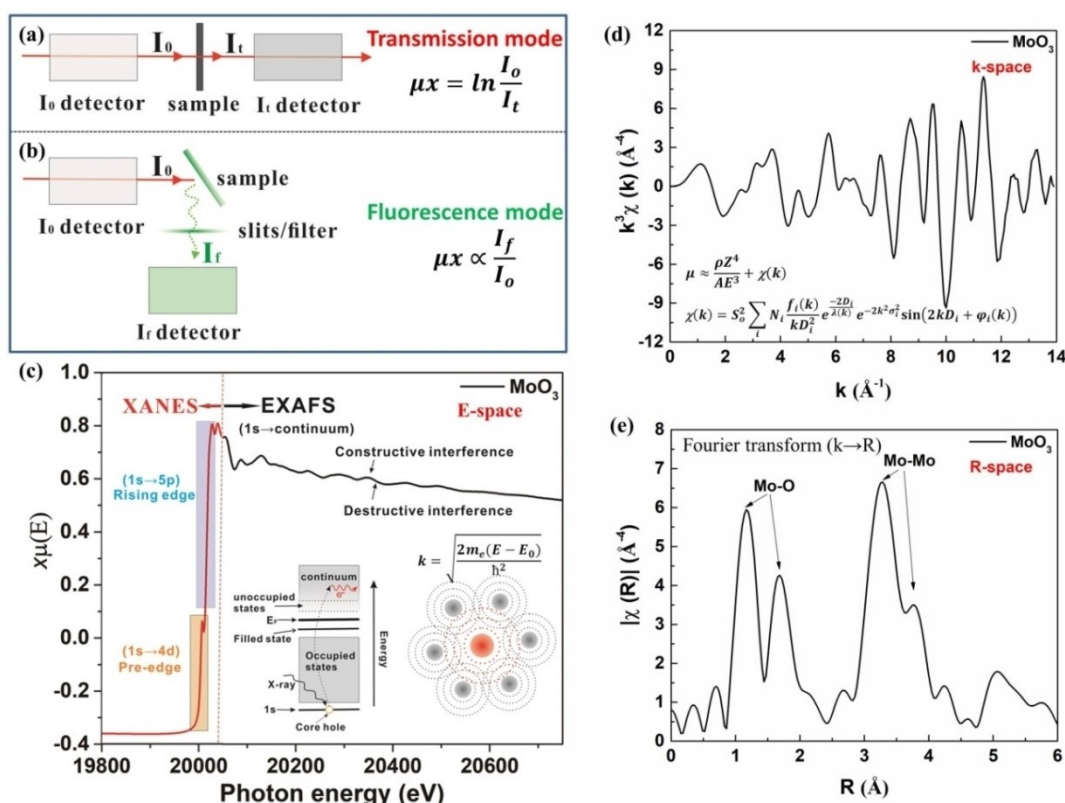
Figure 2. a, b) Schematic diagrams of XAS experimental set-up in transmission or fluorescence mode. c) Spectral regions of Mo K-edge XAS spectrum based on MoO₃ powder. The inset shows the transitions that contribute to edge and pre-edge jump in XANES part, and multiple scattering effects that contribute to EXAFS oscillations. d) k^3-weighted Mo K-edge EXAFS oscillations and e) FTs of k^3-weighted Mo K-edge EXAFS oscillations of MoO₃ powder.

Batteries & Supercaps

Review

doi.org/10.1002/batt.202100006

Chemistry
Europe

European Chemical
Societies Publishing

into the vacuum continuum. This absorption behavior can be quantified by comparing the intensity of the incident beam (I_o) to that of the transmitted beam (I_t), or by comparing the intensity of the incident beam (I_o) to that of the fluorescence (I_f) given off by the excited atoms as an electron fills the now-vacant core orbital (the core hole), or by comparing the intensity of the incident beam (I_o) to that of the ejected electrons as the core hole is filled (Auger electrons).[23]

In a transmission experiment, μ or μx can be calculated by Eq. (1):

$$\mu x = \ln \frac{I_o}{I_t} \tag{1}$$

In a fluorescence experiment, μ or μx can be calculated by Eq. (2)

$$\mu x \propto \frac{I_f}{I_o} \tag{2}$$

where μ denotes the x-ray absorption coefficient, x denotes the sample thickness, I_o denotes the intensity of incident beam, I_t denotes the intensity of transmitted beam, I_f denotes the fluorescence intensity, and μx denotes the absorption length.

Transmission mode is the most convenient way to collect XAS data with good data quality (high signal-to-noise ratio), especially when samples are concentrated, whilst fluorescence mode is required when samples are dilute (typically $< 0.5\%$ of the element of interest). The sample is in line with the two ion chambers monitoring the incident beam intensity I_o and the transmitted beam intensity I_t in transmission mode (Figure 2a), whilst the sample is placed at 45° towards both the incident beam and the fluorescence detector in fluorescence mode (Figure 2b).

An XAS spectrum, consisting of X-ray absorption near edge structure (XANES) and extended X-ray absorption fine structure (EXAFS), can be generated by stepping through an energy range whilst determining the fraction of X-ray photons absorbed at each energy point, probing both the electronic structure and local geometry of matter (Figure 2c).[23a,24] The XANES part of the XAS spectrum probes the unoccupied bound states accessible to the given absorbing atom in matter, which can provide electronic information including oxidation state, geometry configuration, and chemical specificity. The EXAFS part reflects excitations of photoelectrons into the continuum, which can provide quantitative local structure information of matter, including bond distances, bond angles, coordination numbers, neighboring atom types and degree of disorder, with reasonable accuracy.[25] Figure 2c shows the Mo K-edge X-ray absorption spectrum of MoO_3 and a conceptualization of the X-ray absorption process, where the XANES part refers to the spectrum near the rising absorption edge between about -50 and 200 eV relative to the absorption edge energy, whilst the EXAFS part refers to the oscillatory part of an absorption spectrum beyond the absorption edge up to approximately 1000 eV or greater.[26]

The shape of the absorption edge is closely related to the density of states available for the excitation of a photoelectron. Consequently, the XANES spectrum can provide information on the binding geometry and the oxidation state of the absorber atom. Due to electronic screening effects, the position of the edge will shift towards higher photon energies when the nominal valence of the absorber increases. Below the rising absorption edge, any pre-edge features can also be used as a marker for the local geometry and oxidation states.[27]

The constructive and destructive interferences between the outgoing and backscattered photoelectron waves give rise to the periodical sinusoidal variation of μ vs. E, which is known as EXAFS. As shown in Figure 2c, when X-rays are absorbed by a core-level electron, a photoelectron with wavevector k is ejected and propagates away from the absorber atom as a spherical wave (the red lines). The wavevector k is closely related to the excess photon energy $E-E_0$, which can be expressed by Eq. (3),

$$k = \sqrt{\frac{2m_e(E-E_0)}{\hbar^2}} \approx \sqrt{\frac{E-E_0}{3.81}} \tag{3}$$

where k represents the wavenumber, m_e represents the mass of an electron, $\hbar$ represents the reduced Plank's constant, E represents the incident photon energy and E_0 represents the threshold (edge) energy.

If the absorber atom is isolated, the absorption coefficient μ will depend on the sample density ρ, atomic mass A, atomic number Z, and X-ray energy E, which can be expressed by the Eq. (4),

$$\mu_0 \approx \frac{\rho Z^4}{AE^3} \tag{4}$$

If the absorber atom is coordinated, the absorption coefficient μ can be expressed by Eq. (5),

$$\mu \approx \frac{\rho Z^4}{AE^3} + \chi(k) \tag{5}$$

After a series of approximations, the normalized oscillatory component of the absorption coefficient above the absorption edge can be expressed by Eq. (6),

$$\chi(k) = S_o^2 \sum_i N_i \frac{f_i(k)}{kD_i^2} e^{\frac{-2D_i}{\lambda(k)}} e^{-2k^2\sigma_i^2} \sin(2kD_i + \varphi_i(k)) \tag{6}$$

where S_0^2 is the amplitude reduction factor and accounts for the shake-up/shake-off processes of the absorber atom. N_i denotes the coordination number of the absorber atom, where the N_i neighboring atoms are at the same coordination distance D_i away. $f_i(k)$ is the background scattering amplitude of the i-type atom and depends on the nature of the scattering atoms. σ_i^2 is the Debye-Waller factor, and it estimates the variance in D_i due to thermal vibrations and static disorder. $\lambda(k)$ is the mean free path of the photoelectron and $\phi_i(k)$ is the phase shift of the photoelectron.[28]

By modeling the EXAFS signal, it can be used to quantify the local atomic structure of the absorber in terms of short range order, offering structure information related to the numbers and types of coordinated atoms, their interatomic distances, and the degree of structural (and thermal) disorder.

2.2. Analysis of XAS Spectrum

To access these structural parameters in an experimental XAS spectrum, typical software modules, such as the Athena and Artemis programs in the Demeter package running IFEFFIT computation code, are widely used for data analysis, processing, and fitting.[29] Pre-processing of the spectra, such as calibrating, aligning, merging, deglitching, and truncating data groups, can be performed, depending on the data quality. The data analysis procedures mainly involve background removal, normalization, conversion to k-space (Figure 2d), Fourier transform to R-space (Figure 2e), and reverse Fourier transform and fitting. Data analysis methods such as linear combination fitting (LCF), principle components analysis (PCA) and peak fitting can be performed with the Athena software. LCF can be used to interpret the kinetics of series of spectra and deduce the reaction rate during a redox reaction, and determine the species and quantities of standards in a heterogeneous sample by fitting a linear combination of standard spectra to unknown spectra. PCA can be used to analyze the principle components by decomposing a data sequence abstractly. Peak fitting is an empirical analysis technique that can be used to quantify the variation of certain spectral features in a sequence of data by fitting a number of analytical line shapes to XANES data.[30] It is worth mentioning that the multivariate curve resolution-alternating least square (MCR-ALS) approach, as a new chemometric method, is advantageous to extract unbiased, chemically meaningful components from large spectroscopic datasets.[31]

In particular, Fourier transforms (FTs) can be used to visualize the constituent frequencies contributing to the EXAFS spectrum, so the transformation from k space ($\mathring{A}^{-1}$) to R space ($\mathring{A}$) generates a radial distribution function of coordination distances with uncorrected phase shifts. Based on the EXAFS formula of Eq. 6, an EXAFS fit can provide quantitative local atomic structure information through a curve-fitting procedure using the Artemis program.[23b] To fit these structural parameters, the EXAFS spectrum was first converted from $\chi(E)$ in E space to $\chi(k)$ in k-space, then the $\chi(k)$ data is weighted by k^w ($w = 1$ or 2 or 3) to weight the components at different k value. The weighted $k^w\chi(k)$ function was Fourier transformed to R space to provide a radial distribution function of the coordination environment around the absorption atom. The EXAFS simulations were then performed using the Artemis software package with the FEFF6 algorithm. Based on Eq. 3 and Eq. 6, the EXAFS structural parameters remaining to be simulated includes E_0 (the energy shift, ≤ 10 eV), S_0^2 (the scale factor, accounting for multielectron effects ranging between 0.7 and 1.05), N_i (the degeneracy for the ith path), ΔD_i (change in half-path length, less than 0.5 Å), σ_i^2 (Debye-Waller factor, also known as disorder factor, ranging between 0.002 and 0.03 Å^2,

represent the square of the standard deviation of the half path length). In addition, those parameters including $f_i(k)$ (effective scattering amplitude), $\phi_i(k)$ (effective scattering phase shift), $\lambda(k)$ (mean free path) and D_0 (initial half path length, $D_i = D_o + \Delta D_i$) can be calculated by the FEFF code.[29]

To fit these structural parameters that determine the amplitude of EXAFS oscillations (N_i, S_0^2, σ_i^2) and the phase of the EXAFS oscillations (E_0 and ΔD_i), one should consider the following constraints,[26]

ΔD_i: (i) The change in path length parameters can be defined by using a symmetric expansion term as alpha*reff; (ii) Values can be grouped depending on distance and atom types; (iii) Values can be related to unit cell dimensions or atomic moieties; (iv) Values can be determined independently for each path.

E_0: (i) Energy shifts can be depending on atom types (ii) One energy shift can be used for all paths; (iii) Two energy shifts, one for the first shell and another for all other shells, can be applied.

σ_i^2: (i) Values can be grouped depending on distance and atom types; (ii) Values can be described by a Debye or Einstein model, with one or more characteristic temperatures; (iii) Values can be independent for each shell; (iv) Values can be separated into two components to represent the structural and thermal disorder in the bond lengths.

S_0^2: (i) One value of S_0^2 is often used for all paths; (ii) S_0^2 value can be obtained by fitting the measured EXAFS spectra of standards; (iii) Theoretical calculations (by FEFF 8.4 for example) can also be used to determine S_0^2.

N_i: (i) The degeneracy of a path can be determined by the known crystal structure; (ii) Coordination number can also be determined by fitting a data series where N_i is expected to change for each path.

However, how can we determine which fit is better?

x^2, known as "goodness of fit", can be used to quantify the mismatch between the experimental data and fit at each point, which is normalized by measurement uncertainty ε_i, as shown in Eq. (7),

$$\chi^2 = \frac{N_{idp}}{N} \sum_{i=1}^{N} \frac{(f_i^{exp} - f_i^{fit})^2}{\varepsilon_i^2} \tag{7}$$

The validity of two fits on the same set of data can be judged by the reduced-chi-square χ_v^2 [Eqs. (8), (9), (10)],

$$\chi_v^2 = \frac{\chi^2}{v} \tag{8}$$

$$v = N_{ind} - N_{vary} \tag{9}$$

$$N_{idp} = \frac{2\Delta k \Delta R}{\pi} = \frac{2(k_{max} - k_{min})(R_{max} - R_{min})}{\pi} \tag{10}$$

where v is the number of degree of freedom in the fit, N_{ind} is the number of independent points, N_{vary} is the fitting variables.

Although χ_v^2 cannot be used to compare fits on different data (such as different k-ranges from the same data set), it is useful to determine fits to the same data that may differ in the number or identity of free parameters, or in the range of Fourier transform used. A better fit should have a reduced value of χ_v^2, and the ideal value for χ_v^2 is 1 but it is larger than 10 in general owing to a poor estimation of true measurement uncertainties.

Additionally, EXAFS R-factor can be another common method to judge the goodness of the fit, as shown in Eq. (11).

$$R = \frac{\sum_i (f_i^{exp} - f_i^{fit})^2}{\sum_i (f_i^{exp})^2} \tag{11}$$

If the R-factor is small, then the fitted model is very similar to the data. The R factor is proportional to χ_v^2. A good fit generally has a R-factor lower than 0.02, but we should not chase too much on R-factor to the point of preferring 0.001 to 0.002.

The Hamilton test based on Eq. (12) can be utilized to determine if one model can be rejected in favor of another.

$$I_r(a, b) = \frac{\int_0^r t^{a-1}(1-t)^{b-1}dt}{\int_0^1 t^{a-1}(1-t)^{b-1}dt} \tag{12}$$

where r is the ratio of the R-factor for the closer fit to that for the further fit, a is half the lower bound of the number of degrees of freedom of the closer fit, b is half of the number of free parameters that added to switch from the further fit to the closer fit.

Whilst the Hamilton test is only suitable for comparing two fits on the identical k- and R-ranges with different models, reduced χ_v^2 can be used to compare fits on two different R-ranges.

In conclusion, to evaluate how good a fit is, there are eight criteria to follow with, including χ_v^2 (used to determine which fit is better when two fits are on the same data), R-factor, precision of parameters of interest, size of data ranges, agreement beyond the fitting ranges, stability, whether the result is physically possible, and the defensibility of the model (with characteristics of simplicity and/or flexibility and/or physical accuracy).[23a]

2.3. Advantages of XAS

Synchrotron light sources have natural advantages of high brilliance, broad tunable wavelength, high collimation, low emittance and the polarization of synchrotron radiation, enabling researchers to conduct *in situ/ex situ*, element-selective, and qualitative/quantitative experiments at the XAS beamline end station efficiently and accurately.[32] In comparison to any laboratory XAS instruments, synchrotron XAS advantageous to high energy resolution and high throughput allows quick collection of spectroscopic data to record atomic structure and/or oxidation state variation that occur on short time-scales and in confined spaces achieving a good signal-to-noise ratio. Since electrochemical reactions involve phase transitions and redox reactions that involve great complexity, XAS is a suitable and often essential tool to characterize the electrochemical reaction mechanisms of rechargeable batteries by probing the electronic structure and local structure of selected elements of matter.[24] It can be advantageous to detect charge transfer, oxidation states, and short-range atomic structure of the electrode materials, where other tests, such as XRD and TEM, could not tell the full story. In comparison with other localized probes such as TEM, synchrotron XAS is advantageous to average the local atomic structure of a sample area over several square millimeters, which makes it statistically more reliable. High energy synchrotron X-rays with high penetration and weak interaction with electrode materials will not perturb the electrochemical reactions in operating cells, in contrast to the *in situ* SEM/TEM studies where strong interaction between electron beams and battery materials may alter the battery operating states. Besides, XAS can be applied to all states of matter, no matter whether they are in the solid, liquid or gaseous state, thus allowing accurate investigation of a large variety of materials. In particular, it can probe the local structure of both amorphous and crystalline phases, identify the local repartition of a solid solution, and provide local atomic information even on single-atom or two-dimensional materials. It can also be used to study solid-state or liquid-state electrolytes for rechargeable batteries.[27,33] Due to its elemental specificity and the high penetration of synchrotron X-rays in the range of 4–100 keV, XAS is suitable for studying battery materials in real time by using customized *in situ* electrochemical cells.[33a] *In situ* or *operando* XAS characterization of the whole electrode system can be realized by directing X-rays through an apertured coin-cell to interact with the active material. These spectroscopic results, together with the corresponding electrochemical data and complementary analytical tools, can provide comprehensive insights into the electrochemical reaction mechanisms, thus guiding the design development of next-generation electrode materials for rechargeable batteries.

In brief, the versatility of synchrotron XAS can be summarized as follows,[33a]

(i) Synchrotron XAS enables the study of electronic and local structure information, including charge transfer, oxidation states, site symmetry, degree of disorder, and bonding number, length, angle, and species that are involved in the electrolytes and electrode materials, regardless of whether they are in the crystalline, amorphous, solid, or liquid state;

(ii) The element-selective flexibility of the synchrotron XAS beamline enables a wide range of elements to be studied in local view, while the concentration-sensitive fluorescence mode enables low-concentration components (sub-ppm level) to be studied in electrodes;[34]

(iii) The high throughput of synchrotron beamlines, endowing it with excellent data quality (high signal-to-noise ratio) and rapid data recording speed (up to several seconds per

Batteries & Supercaps

Review
doi.org/10.1002/batt.202100006

Chemistry Europe
European Chemical
Societies Publishing

spectrum), which are dedicated to high precision *in situ* and *operando* electrochemical studies;

(iv) Systematic and consistent data analysis, such as principal component analysis, wavelet transform, multivariate curve resolution-alternating least squares, and EXAFS fitting, provides reliable data reduction to explain the experimental spectra in a qualitative/quantitative way.

However, there are also some limitations of the XAS technique, including (1) as a stand-alone technique XAS is not necessarily able to differentiate small clusters from single atoms;[35] (2) partially overlapping edges and emission lines can limit the useful energy range in mixed samples (materials containing both Mn and Fe for example); (3) *in situ* cycling of materials over long time periods may cause beam damage/ chemical changes within the material that may complicate data interpretation.[36]

2.4. In Situ Synchrotron XAS Experimental Design

Time-resolved high-flux synchrotron XAS measurements can provide dynamic electronic and local atomic structure information of selected elements of electrode materials during battery operation. Since battery mechanisms involve phase changes and redox reactions that lead to great complexity, such as unexpected transient and/or metastable phases, *in situ* synchrotron XAS can be used as a cutting-edge technique with high energy/temporal/spatial resolution to characterize electrochemical reactions and kinetics for rechargeable batteries. *Ex situ* XAS measurements can only grasp part of valuable information from batteries since they may suffer from adverse conditions during disassembling, including side reactions caused by air exposure, short circuit caused by dismantling, and unreliable intermediate phases caused by altered electrochemical environments, which poses great challenges to understand the exact electrochemical reaction mechanisms and kinetics during battery operation.[15a] In contrast, *in situ* XAS experiments can provide real-time spectroscopic information of an operating customized cell by probing the photon intensity change when X-rays penetrate through the electrode in the transmission mode, or via X-ray fluorescence emitted from the electrode in a fluorescence mode setup.

A brief scheme of *in situ* XAS experiments is presented in Figure 3, which describes the *in situ* XAS experiment conducted at the Australian Synchrotron via a transmission mode setup.[37] The initial X-ray beam from the synchrotron source is tuned by a crystal monochromator to select a particular photon energy range. Then, the incident X-ray beam passes through a gas filled ion chamber to determine the incoming signal strength (I_0) before interacting with the apertured coin-cell. The apertured coin-cell can be shifted freely by a liquid jet system, which is mounted on a three-axle translational motor stage. Another ion chamber is mounted linearly towards incident X-ray beam for the detection of transmitted X-ray beam (I_t).[38] The use of gas composition for the ion chambers is energy-dependent.[39] Additionally, a standard reference is measured simultaneously with the *in situ* coin-cell so as to calibrate the
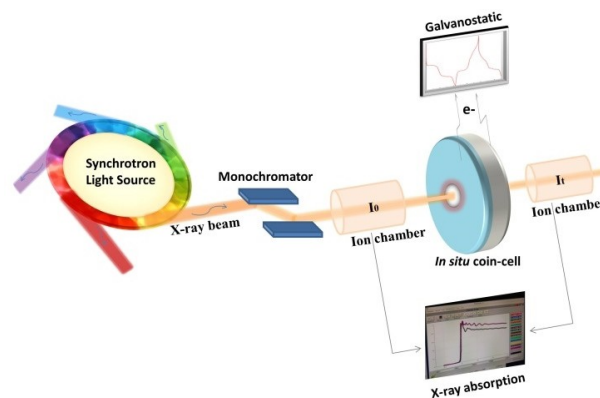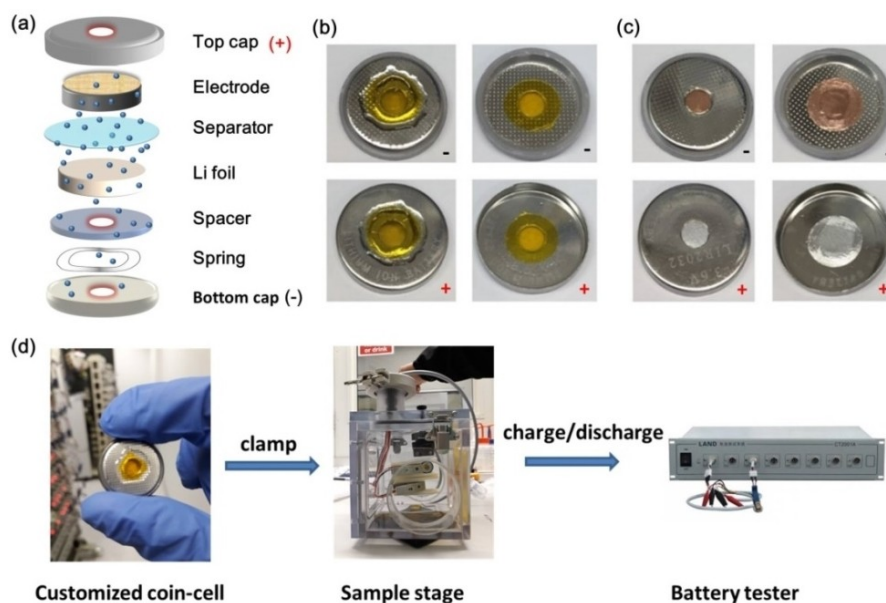

Figure 3. Schematic illustration of *in situ* XAS experiments conducted in the transmission mode for rechargeable batteries.

photon energy E_o and align the spectra thereafter. Moreover, other experimental references should also be prepared accordingly so as to fingerprint spectral features for use in LCF, PCA and so on.

As shown in Figure 4a, apertured CR2032 coin-cells were customized herein, where 5 mm holes were punched on positive and negative caps, as well as in the spacer, to allow the transmission of synchrotron beam. To cover the holes of caps, there are several typical windows to choose from, including Be foil and polyimide film (Kapton® tape), which completes a seal with the help of an epoxy adhesive (Figure 4b). Although X-ray transparent Be foil have better hardness and conductivity than Kapton® tape, the toxicity, the nature of alkaline-earth metals, and electrochemical instability at high potential limit its practical application as windowing material. Kapton® tape benefits from its low cost and from being non-hazardous X-ray transparent, but it is electrically insulative, and tends to soften over time (Figure 4b). Recently, our group developed a facile and low-cost metal-tape coin cell, using Al tape and Cu tape as covers, for *in situ* synchrotron X-ray diffraction and XAS experiments, which can ensure good conductivity, tightness and sealing, and even work well during high-voltage operation (Figure 4c).[40] It is noted that Cu tape is not that appropriate to test some of the anode materials *in situ*, especially when targeting lighter metallic elements such as Ti, Ni and Ge. For higher energies on the other hand, such as the Sn and Sb K-edges, either Al or Cu tapes will work well. One should carefully take into account that the fraction of the photon intensity that makes it through the sample is exponentially dependent on the number of absorption lengths present (Bouguer's Law).[41]

Other cell components are similar to conventional coin-cells, but care must be taken to the as-synthesized working electrodes. Firstly, with regard to current collectors used for *in situ* hard XAS study, carbon cloths are versatile substrates for coating anode materials as the working electrode with negligible absorption of photon intensity for hard X-ray. But it may suffer poorer signal-to-noise in transmission mode if electrode materials are not uniformly distributed in the matrix. Aluminum foils can be excellent current collectors when

Batteries & Supercaps

Review
doi.org/10.1002/batt.202100006

Chemistry Europe
European Chemical
Societies Publishing

Figure 4. a) Schematic illustration of an apertured coin-cell for *in situ* synchrotron XAS experiments. Cell caps sealed by b) the Kapton®-window and (c) the metal-tape-window. d) Experimental program and configurations for the *in situ* XAS experiments conducted at the X-ray absorption spectroscopy beamline at the Australian Synchrotron. Reproduced from Ref. [40] with permission. Copyright 2020, Wiley-VCH.

studying insertion-type anodes (operating voltage beyond 1.0 V). Ni foil and Cu foil can be suitable for studying heavy elements such as Sn and Sb in transmission experiments, but it will be problematic when studying lighter elements such as Ti and Ge since few x-ray photons will get through near the K-edge of Ti or Ge. Secondly, the mass loading of the active materials on the electrode used for *in situ* XAS measurement should be optimized to satisfy an optimal edge jump for the relevant absorption edge. Last but not the least, the material should be distributed as uniformly as possible so as to avoid distortion of the data, and the particle size of the active material should be less than approximately 0.2 absorption length.[23a]

An *in situ* electrochemical device setup for the XAS end station used at the Australian Synchrotron is shown in Figure 4d. Firstly, customized coin-cells were clamped by battery clips in a customized sample holder, and the holder was then mounted on the three-axle translational motor stage. The *in situ* electrochemical device is ready to use when connected with a battery tester, and the charge-discharge process can be controlled by a computer. It allows up to three coin-cells to be operated simultaneously, making efficient use of facility time for data collection. The homogeneity of the sample should be checked before running the electrochemical tests.

Apart from the *in situ* cell design mentioned above, other cell configuration including pouch-type cells, Swagelok-type cells, and "coffee bag"-type cells can also be applicable accordingly for *in situ* XAS measurement.[42] However, it is critical to consider the amount of electrode materials used, the window covered, and the current collector applied so as to ensure a high spectral quality.

Time-resolved *in situ* synchrotron XAS experiments can be performed quickly (as fast as tens of seconds per spectrum) by collecting XANES spectra only to understand the dynamic charge transfer, oxidation states, and local geometry of the electrode. *In situ* EXAFS spectra, whose collection is more time-consuming (more than several minutes per spectrum), can also be collected to provide quantitative local structure information in detail.

3. In Situ XAS Studies of Battery Anodes

Synchrotron XAS has been widely used to study rechargeable batteries, including its cathodes, anodes and electrolytes. XAS-based studies on cathode materials have been summarized by several reviews,[17a,43] whilst herein we will focus on anode materials which were studied using *in situ* XAS measurements. Anode materials can be typically divided into three types, namely insertion-type, alloying-type, and conversion-type anodes. Recent progresses are summarized in Table 1.

3.1. In Situ XAS Studies of Insertion-type Anodes

Insertion-type anodes accommodate lithium-ions or other metal-ions reversibly within accessible host structures, during which redox reactions and small volume changes occur with the main crystal framework remains stable. Beyond graphite, insertion-type anodes such as Nb_2O_5, TiO_2, and $Li_4Ti_5O_{12}$ are also promising anodes for LIBs due to their extraordinary high-rate capability and/or long cycling life originating from their unique structural characteristics.[68] Synchrotron XAS can be an advanced technique to track the valence states of redox centers, the local geometry symmetry, and the reversibility of

Table 1. A summary of *in situ* XAS experiments conducted for battery anodes.
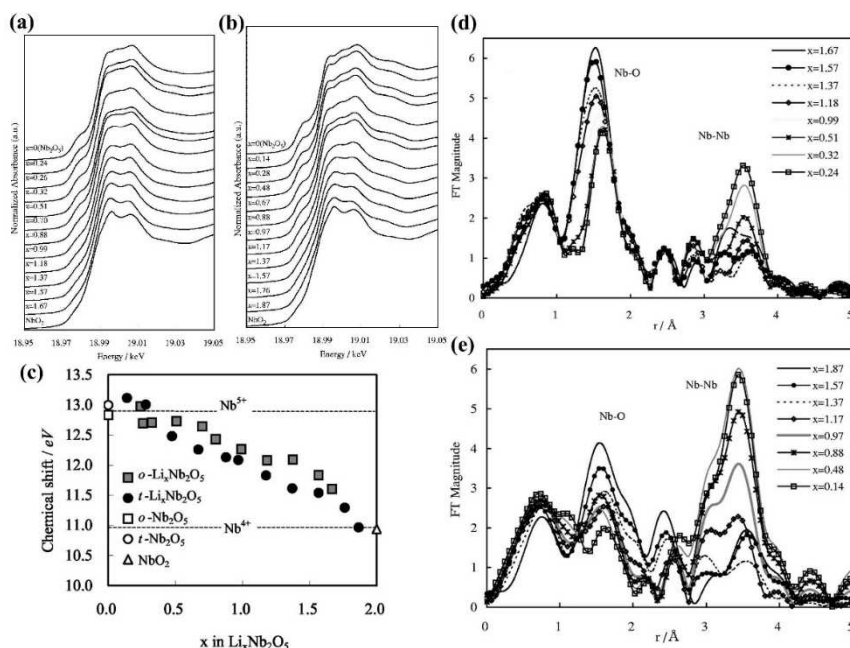
Anode Materials	Edges	Mode[a]	*In situ* cell types	Analysis Results	Ref.
Nb_2O_5	Nb K	T	Pouch-type LIBs	Redox reaction; local structure variation	[44]
$Nb_{16}W_5O_{55}$	Nb K	T	AMPIX LIBs	Redox reaction; local structure variation	[45]
$Nb_{18}W_{16}O_{93}$	W L_{III}				
$Li_4Ti_5O_{12}$	Ti K	F	Coin-type LIBs	Redox reaction; local structure variation	[46]
TiO_2	Ti K	T	Coin-type LIBs	Redox reaction; contribution of surface storage	[47]
TiO_2	Ti K	F	Coin-type SIBs	Redox reaction; local structure variation	[48]
Sn	Sn K	T	Pouch-type LIBs	Local structure variation	[49]
Sb	Sb K	T	Coin-type SIBs	Local structure variation; amorphous intermediates	[50]
Ge	Ge K	T	Pouch-type LIBs	Local structure variation and amorphous intermediates	[51]
SnSb	Sn/Sb K	T	Swagelok-type SIBs	Local structure variation and phase compositions	[52]
$Bi_{0.5}Sb_{0.5}$	Bi L_{III} Sb K	T	Swagelok-type SIBs	Local structure variation and amorphous intermediates	[53]
TiSnSb	Ti/Sn/Sb K	T	Swagelok-type LIBs	Local structure variation; reversibility; components	[54]
SnO_2	Sn K	F	Coin-type LIBs	Redox reaction; structure variation; phase components	[55]
Mn_3O_4	Mn K	T	Coin-type LIBs	Redox reaction; structure variation; phase components	[56]
Sn_4P_3	Sn K	F	Coin-type LIBs	Local structure variation and reversibility	[57]
SnS_2	Sn K	T	Coin-type SIBs	Local structure variation	[58]
MoS_2	Mo L S K,	F	Coin-type LIBs	Local structure variation and reversibility	[59]
$Ge_{0.9}Se_{0.1}$	Ge/Se K	T	Coin-type LIBs	Amorphous Li–Se–Ge phase evolution	[60]
Fe_3O_4	Fe K	T	Coin-type LIBs	Reaction pathway and phase evolution	[61]
$(Mg_{0.2}Co_{0.2}Ni_{0.2}Cu_{0.2}Zn_{0.2})O$	Cu/Ni/Co K	F	ECC-Opto-Std test LIBs	Species and concentration evolution	[62]
$(Ni_{0.2}Co_{0.2}Mn_{0.2}Fe_{0.2}Ti_{0.2})_3O_4$	Ni/Co/Mn/Fe K	F	Coin-type LIBs	Local symmetry and oxidation states	[63]
Mo/V poly-oxometalate	Mo/V K	F	Coin-type LIBs and pouch cell	Oxidation state change	[64]
$MoTe_2$	Mo K	F	Coin-type LIBs	Phase evolution	[65]
$Fe_{1-x}S$	Fe K	T	Coin-type LIBs	Electronic changes; structural alterations	[66]
Bi_2O_2Se	Bi L_{III} Se K	T	Coin-type LIBs and PIBs	Redox reactions; species	[67]

[a] T denote transmission, and F denotes fluorescence.

electrode materials for insertion-type electrodes dynamically during battery operation.

Nb-based oxides, including Nb_2O_5 and the Nb–X–O family (X=W, Ti, Cr, Ga, Fe, Mg, etc.), are attractive candidates for high-rate electrochemical energy storage systems with open and stable Wadsley-Roth shear crystal structures.[68b] In 2006, Kodama et al.[44] reported an *in situ* XAS study of Nb_2O_5 anodes for LIBs for the first time (Figure 5). During the initial discharge, the absorption edge of the XANES spectra reveals a continuous shift toward lower photon energy, manifesting the gradual reduction from Nb^{5+} to Nb^{4+} in both Nb_2O_5 phases. In the Fourier transformed EXAFS spectra, the nearest shell at around 1.5 Å correspond to the first Nb–O shell, and the peaks at around 3.5 Å can be ascribed to the Nb–Nb interaction primarily in the second shell. In the case of the tetragonal phase (the *t*-Nb_2O_5 electrode), as lithiation proceeds, the peak intensity of the first Nb–O shell increases significantly whilst the peak intensity of the Nb–Nb shell decreases significantly, due to the insertion of Li into the sites between the two-dimensional layers of the NbO_6 octahedra, which causes a loss of the flatness of the planar arrangement of the Nb atoms and increases the shielding effect of Li against the Nb–Nb interaction. In the case of the orthorhombic phase (the *o*-Nb_2O_5 electrode), the decrease in the peak intensity of the Nb–Nb shell was much less than that for the *t*-Nb_2O_5 electrode, which can be owing to the differential insertion sites between these two phases. The *o*-Nb_2O_5 electrode, with a three-dimensional

framework, may store lithium primarily in the interstitial sites, whilst the *t*-Nb_2O_5 electrode preferentially stores lithium in the interlayer sites, resulting in a higher lithium storage capability. Very recently, $Nb_{16}W_5O_{55}$ and $Nb_{18}W_{16}O_{93}$ were highlighted as high-rate anodes for LIBs, and their redox activity and local geometry were investigated by *operando* XANES and *ex situ* XANES (Figure 6).[45] The $Nb_{16}W_5O_{55}$ electrode demonstrates an approximately linear relationship between the number of electrons (and Li^+) transferred and the oxidation state of niobium during the initial discharge, whereas Nb^{5+} was gradually reduced to Nb^{4+} and Nb^{3+}. It should be noted that the oxidation state of niobium is extracted from the shift of the absorption edge of the *operando* and *ex situ* Nb K-edge XANES spectra. Likewise, *operando* and *ex situ* electrodes measured at the W L_1-edge demonstrated a steadily negative correlation between the number of electrons (and Li^+) transferred and the oxidation state of tungsten, where W^{6+} was gradually reduced to W^{4+}. Both Nb^{5+} and W^{6+} redox centers are coordinated octahedrally and undergo second-order Jahn-Teller (SOJT) distortions, which give rise to obvious pre-edge features before the main absorption edges in the Nb K-edge and W L_1-edge XANES spectra before discharge. During lithiation, the decrease of the pre-edge integrated peak intensity indicates an increase in the local symmetry for the intercalation hosts. To conclude, the XANES edge shifts and pre-edge evolution demonstrate a parallel reduction pathway and multi-electron charge transfer

Batteries & Supercaps

Review
doi.org/10.1002/batt.202100006

Chemistry
Europe
European Chemical
Societies Publishing

Figure 5. *In situ* Nb K-edge XANES spectra of a) o-Li$_x$Nb$_2$O$_5$ and b) t-Li$_x$Nb$_2$O$_5$. c) Chemical shifts of the Nb K-edge spectra *vs.* Li content x in Li$_x$Nb$_2$O$_5$ during lithiation. Radial structure functions of d) o-Nb$_2$O$_5$ and e) t-Nb$_2$O$_5$ electrodes during lithiation, obtained by FTs of the Nb K-edge EXAFS oscillations. Reproduced from Ref. [44] with permission. Copyright 2006, The Electrochemical Society.
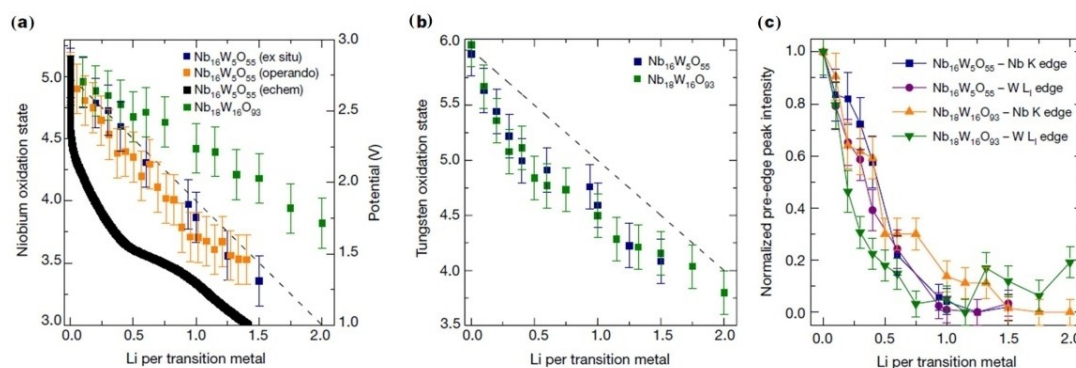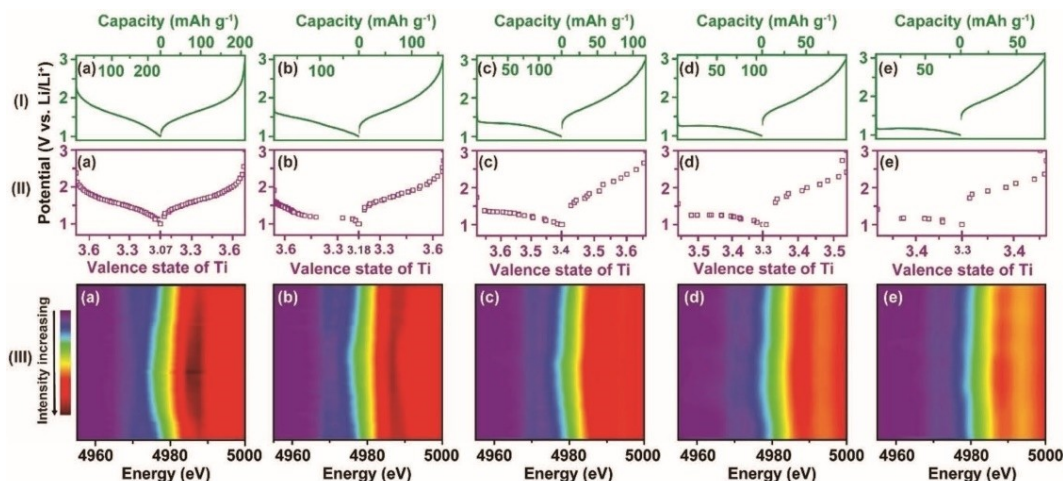

Figure 6. XANES study of Nb$_{16}$W$_5$O$_{55}$ and Nb$_{18}$W$_{16}$O$_{93}$ at the Nb K-edge and W L$_1$-edge. Oxidation states of Nb (a) and W (b) as a function of lithiation, extracted from shifts in the absorption energy of the Nb K-edge and the W L$_1$-edge. c) Pre-edge integrated peak intensity from the Nb K-edge and W L$_1$-edge serves as a measure of local distortion and the oxidation state. Reproduced from Ref. [45] with permission. Copyright 2018, Macmillan Publishers Ltd., part of Springer Nature.

of both transition metals for the Nb$_{16}$W$_5$O$_{55}$ and Nb$_{18}$W$_{16}$O$_{93}$ electrode.

Ti-based oxides such as TiO$_2$, Ti$_2$Nb$_{10}$O$_{29}$, and Li$_4$Ti$_5$O$_{12}$ are also attractive insertion-type anodes for LIBs, owing to their high-rate performance, good cycling stability, safe operating voltage, and low cost.[69] The origin and contribution of surface storage in the TiO$_2$(B) electrode is identified by *in situ* Ti K-edge XANES measurements, with dynamic valence states monitoring at different discharge rates.[47] As shown in Figure 7, the absorption edge in the contour plot shifts towards lower energy during discharge and shifts in the reverse direction during charge, indicating the good structural reversibility of TiO$_2$(B) during cycling. The shifted distance is shortened when the discharge current density is increased. The valence state

evolution curves extracted from the XANES spectra are similar to the corresponding discharge/charge curves at different rates, indicating that the electrochemical behavior is dominated by the faradaic reactions. Coupling with cyclic voltammetry (CV) kinetic analysis, the ratios of pseudocapacitive, non-faradaic, and diffusion-controlled capacities contributed in TiO$_2$ electrodes can be quantitatively evaluated. In addition, the electrochemical lithium-ion storage mechanism of Li$_4$Ti$_5$O$_{12}$ was studied by *in situ* Ti K-edge XANES analysis in the fluorescence mode combined with *ab initio* calculations, demonstrating that structural transformations in spinel Li$_4$Ti$_5$O$_{12}$ during lithiation occur as a multi-stage kinetic process involving a mixed quasi-solid solution and the macroscopic two-phase transformations, which occur both locally and globally (Figure 8). Variations in

Batteries & Supercaps

Review

doi.org/10.1002/batt.202100006

Chemistry
Europe

European Chemical
Societies Publishing

Figure 7. (I) Galvanostatic discharging/charging profiles, (II) the normalized dynamic valence state variations of Ti element, and (III) the corresponding 2D contour plots of Ti K-edge XANES spectra of *in situ* TiO$_2$(B) electrode, which are collected at various current densities of a) 0.075, b) 0.45, c) 0.9, d) 1.25, and e) 1.75 A g^{-1}. Reproduced from Ref. [47] with permission. Copyright 2018, Wiley-VCH Verlag GmbH & Co. KGaA, Weinheim.
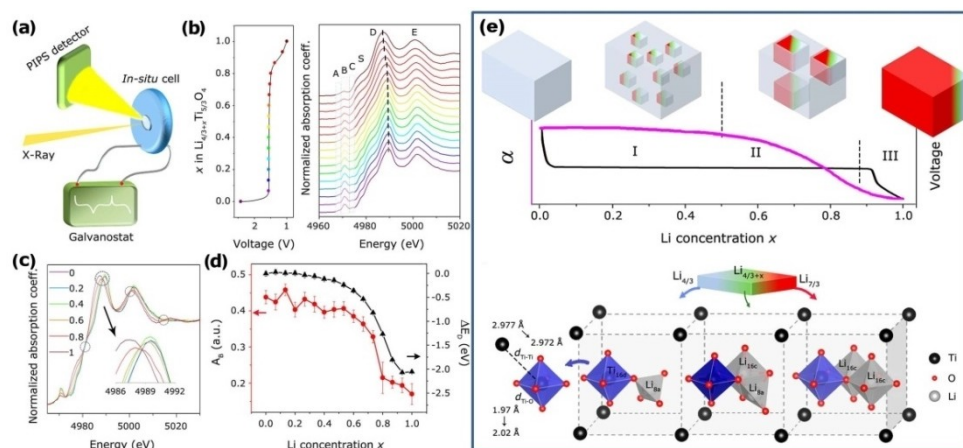
Figure 8. Tracking structural evolution of the lithium titanate (Li$_{4/3}$Ti$_{5/3}$O$_4$) electrode for LIBs by *in situ* XAS. a) Schematic illustration of the *in situ* XAS experimental setup in the fluorescence mode. b) Ti K-edge XANES spectra as a function of Li concentrations (*x*) during the first lithiation at a rate of 0.1 C. c) Selected XANES spectra showing quasi-isosbestic points as marked by black dashed circles. d) Area of the pre-peak B and relative shift of peak D as a function of Li concentration *x*. e) Illustration of the local structural transformations and their correlation to bulk-phase evolution in the Li$_{4/3}$Ti$_{5/3}$O$_4$ electrode. Reproduced from Ref. [46] with permission. Copyright 2017, American Chemical Society.

in situ XANES spectra features can be interpreted by partial reduction of Ti^{4+} to Ti^{3+}, local geometry distortion of TiO$_6$ octahedrons, and Li occupancy at different sites during lithiation. Specifically, the *in situ* cell is covered by Kapton tape window (Kapton polyimide film with Silicone adhesive), uses aluminum meshes as current collectors, and measures in fluorescence mode.[46]

Besides, typical insertion-type anodes for SIBs have also been studied by in situ XAS recently.[48,70] For example, the Na uptake and release mechanism of anatase TiO$_2$ was studied by *in situ* Ti K-edge XANES, which detected decreased original six-coordinated symmetry and irreversible loss of the nanoparticle structural ordering during the first cycle.[48]
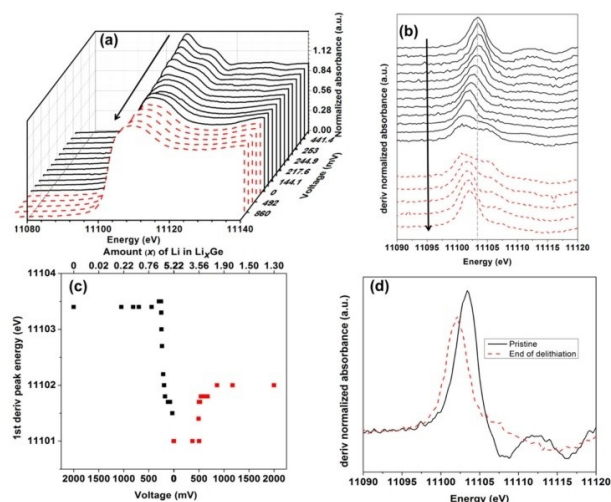
3.2. In Situ XAS Studies of Alloying-type Anodes

Alloying-type anodes have high theoretical capacity, but they suffer from poor cycling stability due to large volume changes during cycling. The electrochemical reaction mechanisms of alloying-type anodes are complex, which often involve charge transfer, local atomic structure changes, and intermediate phases that can be crystalline, poorly-crystalline, or amorphous. Synchrotron XAS can give meaningful insights into the alloying reactions involved in rechargeable batteries by retrieving local atomic structure and electronic information.

For example, Lim et al.[51] studied the electrochemical process of micro-level crystalline germanium (Ge) as anodes for LIBs by *in situ* XAS and XRD measurements, probing both amorphous intermediate phases (by XAS) and crystalline intermediate phases (by both XRD and XAS) during lithiation/

Batteries & Supercaps

Review

doi.org/10.1002/batt.202100006

Chemistry
Europe
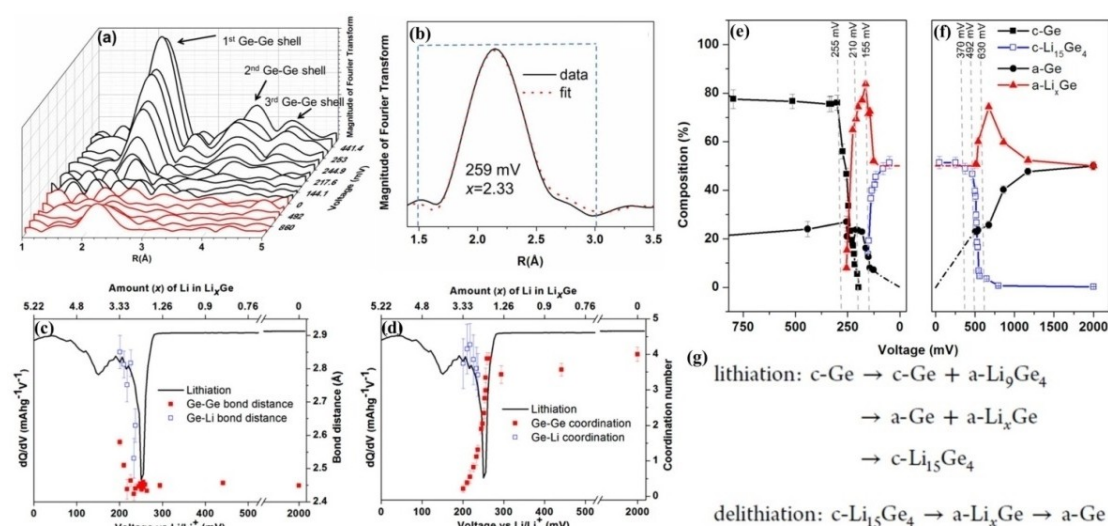
European Chemical
Societies Publishing

delithiation. The XANES spectra data set of the initial cycle is presented in Figure 9. As lithiation proceeds, the sharp white-line feature becomes broader, indicating a decreasing concentration of 4p electronic states, owing to the amorphization and/or phase transitions of germanium. As delithiation proceeds, the white-line intensities of the XANES spectra data set remain broad until the end of delithiation. The corresponding first-derivative of the XANES spectra shows a peak shift towards lower energy during lithiation, then towards higher energy during delithiation, indicating that charge transfer occurs reversibly between Ge and Li during lithiation/delithiation. The peak position of the first-derivative spectrum at the end of delithiation was only partially recovered in comparison to the pristine germanium electrode, which could be owing to the residual lithium bonded to amorphous germanium and/or the excess negative charges from dangling bonds in amorphous germanium. FTs of the EXAFS spectra data set were studied to gain deeper insights into the electrochemical reaction mechanisms that occur during battery operation (Figure 10). The result shows that the intensity of the first, second, and third Ge−Ge shells decreases and disappears gradually during lithiation. During delithiation, only the first Ge−Ge shell partially recovers, whilst the further shells do not recover, indicating that Ge becomes amorphous at the end of the delithiation. The EXAFS spectra were simulated to provide quantitative structural details about bond distances and numbers. As lithiation proceeds beyond 220 mV, the Ge−Ge bond distance stays almost constant at 2.44 Å, and the coordination number of the Ge−Ge bond decreases sharply, whilst the coordination number of the Ge−Li bond increases (due to the generation of diamond-cubic Ge and a-Li_9Ge_4). After that, the Ge−Ge bond distance elongates quickly from 2.44 Å to 2.60 Å (due to the generation of a-Li_7Ge_2). By correlating $in\ situ$ XAS and XRD studies with electrochemical data, the electrochemical reaction mechanism involving amorphous Li_xGe intermediates is elucidated and illustrated in Figure 10e–g. Furthermore, Silberstein et al.[71] also investigated the electrochemical reaction mechanism of Ge nanowires for Li-ion storage by using $operando$ XAS and XRD, revealing that heterogeneous lithiation of the Ge nanowires occurs preferentially in amorphous regions over crystalline domains, and a shallower cut-off voltage can preserve the crystalline structure of the electrode for several

Figure 9. a) Normalized $in\ situ$ Ge K-edge XANES spectra during the course of lithiation (black solid lines) and delithiation (red dashed lines). b) Corresponding normalized first derivatives of the XANES spectra for lithiation (black solid lines) and delithiation (red dashed lines), c) plot of the first derivative peak energy position as a function of voltage and amount (i) of Li in Li_xGe phase, and d) comparison of the first derivative spectrum before lithiation (black solid line) and at the end of delithiation (red dashed line). Reproduced from Ref. [51] with permission. Copyright 2014, American Chemical Society.

Figure 10. Evolution of a) FTs of the Ge K-edge EXAFS spectra during lithiation (black) and delithiation (red). b) A typical fit for the 259 mV data ($x = 2.33$) with a Ge−Ge shell. c) Bond distances and d) coordination numbers for Ge−Ge bonds and Ge−Li bonds obtained by EXAFS fitting, with superimposed differential capacity plots. e, f) A summary of the phase evolution and g) the proposed reaction steps of the crystalline Ge electrode during lithiation/delithiation. ("c" denotes crystalline and "a" denotes amorphous, while a-Li_xGe is composed of Li_9Ge_4, Li_7Ge_2, and LiGe). Reproduced from Ref. [51] with permission. Copyright 2014, American Chemical Society.

Batteries & Supercaps

Review
doi.org/10.1002/batt.202100006

Chemistry
Europe
European Chemical
Societies Publishing

cycles. Interestingly, both XAS studies on Ge anodes for LIBs show different degrees of recovery in the local atomic structure upon full charge, which could be owing to the size effects of the pristine Ge electrodes (nanowires *vs.* micro-level particles) that lead to different degrees of electrochemical reversibility.

The alloying mechanism of the Sn electrode as an anode for LIBs was also studied by *in situ* XAS test.[49] During lithiation, an obvious edge shift towards higher photon energy can be observed, indicating the charge transfer from Sn to Li when lithium is incorporated with Sn. Dynamic changes of the local atomic environment around Sn atoms, including the number, distance, and type of neighboring atoms, are identified by the EXAFS fitting, which provides quantitative information on the local structural changes of the Sn electrode during the initial lithiation.

In addition to mono-metallic anodes such as Sn,[49] Sb,[50] and Ge,[51,71] multi-metallic anodes, such as Cu₂Sb,[72] CoSb₃,[73] NiSb₂,[74] Sn₂Fe,[75] BiSb,[53] and TiSnSb,[54] were also investigated by XAS for chargeable batteries. For instance, Fehse et al.[54] conducted an *in situ* triple K-edge XAS study on TiSnSb anodes for LIBs, including the Sn-, Sb-, and Ti K-edges, revealing that both Sn and Sb are electrochemically active, whilst Ti is inactive for redox reactions but experiences reversible structure changes between TiSnSb and Ti nanoparticles (Figure 11). Regarding XANES (Figure 11a,d,g), insignificant shift of the edge position in the Ti K-edge spectra and considerable edge shift in both Sn- and Sb K-edge spectra can be observed during discharge, indicating that Ti remains in a chemical state close to the metallic one whilst Sn and Sb should be incorporated with lithium showing obvious charge transfer. Regarding EXAFS (Figure 11b,e,h), the EOD component measured at the Sn and Sb K-edge shows rapid decrease in amplitude due to the high share of light scatters (such as lithium), but the EOD component measured at the Ti K-edge do not show similar damping since Ti does not alloy with Li during discharge. The formation of Li_7Sn_2 and Li_3Sb phase upon full lithiation, with a complete amorphization of the structure, is detected, and the electrochemical process is largely reversible after a complete cycle.

Besides, the sodiation process of the $Bi_{0.5}Sb_{0.5}$ alloy was investigated by *in situ* Bi L₃-edge and Sb K-edge XAS collected simultaneously on the same cycling cell.[53] As a complementary tool to XRD, it provides insightful view of the amorphous intermediate phases, that is $Na_yBi_{1-x}Sb_x$ and Na_2Sb, for SIBs. Stievano et al.[52] also investigated the sodiation/de-sodiation process of SnSb alloy by using Sn K-edge EXAFS and Sb K-edge EXAFS. By combing the PCA analysis and the MCR-ALS analysis, the nature and sequence of formation of different species during the sodiation/de-sodiation process have been uncovered.
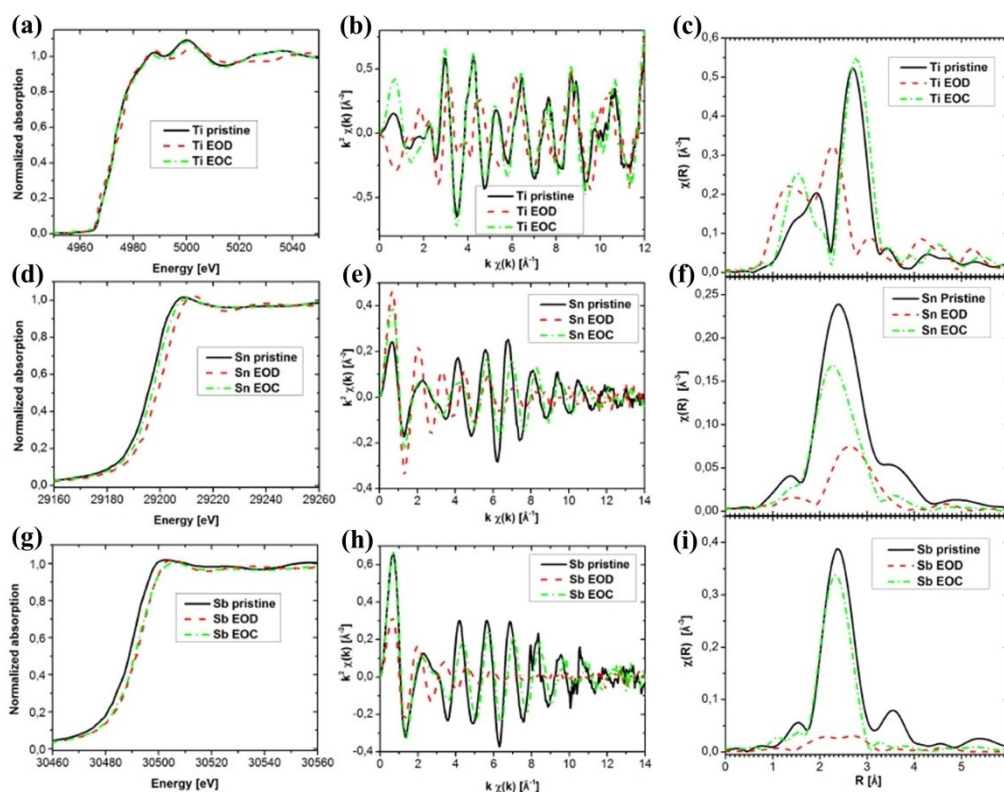

Figure 11. Selected *in situ* XANES spectra (left), EXAFS spectra (middle) and FTs of the EXAFS spectra (right) of the (a–c) Ti (top), (d–f) Sn (middle), and (g–i) Sb (bottom) K-edge XAS spectra collected from the TiSnSb electrode during discharging/charging, which are obtained by multivariate curve resolution-alternated least-squares (MCR-ALS) analysis.[54] EOD denotes the electrode at the "end of discharge", EOC denotes the electrode at the "end of charge". Copyright 2017 American Chemical Society.

Batteries & Supercaps

Review
doi.org/10.1002/batt.202100006

Chemistry Europe
European Chemical
Societies Publishing

3.3. In Situ XAS Studies of Conversion-Type Anodes

Conversion-type anodes, especially metal oxides, chalcogenides, and phosphides, are promising candidates for high-energy-density batteries. They undergo conversion reactions with the generation of new phases, giving rise to high theoretical capacity, but poor cycling stability, and low initial Coulombic efficiency. XAS is advantageous to probe the origin of redox reactions, the character of phase components, and the short-range atomic structure for conversion-type anodes during electrochemical cycling.

The electrochemical reaction mechanisms of metal oxides, such as Mn_3O_4,[56] ZnO,[76] Fe_3O_4,[77] MoO_2,[78] SnO_2,[49] Fe_3O_4,[61] $NiCo_2O_4$,[79] $ZnMn_2O_4$,[80] $ZnFe_2O_4$,[81] and $CuFe_2O_4$,[82] were studied by *in situ* or *ex situ* XAS. For instance, Kim et al.[55] used *in situ* synchrotron XRD and XAS to unravel the detailed lithium storage mechanism of an ordered mesoporous SnO_2 electrode material. Figure 12 presents selected Sn K-edge XANES and EXAFS spectra from five regions of the first cycle. The reduction of Sn^{4+} ions occurs at the start of discharge with a prominent edge shift toward lower energy values in the Sn K-edge XANES spectra set. The corresponding FTs of the EXAFS spectra set show decreasing peak intensity for the first Sn—O shell at around 1.5 Å, as well as further Sn—O and Sn—Sn shells between

2.2 and 3.9 Å, owing to displacement of the reacting species during the conversion reaction. Then, the conversion and alloying reactions take place simultaneously in a sequential way with metallic Sn as an intermediate in the middle discharge region, along with negligible edge shift and significantly decreased white line intensities of the XANES data set. The corresponding FTs of the EXAFS data show steadily decreasing peak intensity of the first Sn—O shell at around 1.5 Å and increasing peak intensity of the further Sn—Sn(Li) shell at around 2.6 Å, due to the decrease in the Sn—O bonds and the increase in the Li/Sn ratio. The alloying reaction between metallic Sn and Li with charge transfer is sustained in the last discharge region of the XANES data set, where the absorption edge shifts toward higher energy values. The corresponding FTs of the EXAFS data show a decreasing Sn—Sn peak and the absence of Sn—O, owing to the further lithiation of the Li_xSn phase towards the final $Li_{4.4}Sn$ phase. Upon charge, the XANES spectra reversibly shift toward lower energies in the first charge region, and the corresponding EXAFS spectra exhibit the rise of Sn—Sn(Li) peaks, indicating that only the dealloying reaction takes place in this potential region. In the last charge region, the XANES spectra show increasing white line intensity but with negligible edge shift, and the corresponding EXAFS spectra show an enhanced Sn—O peak and a damped Sn—Sn(Li)
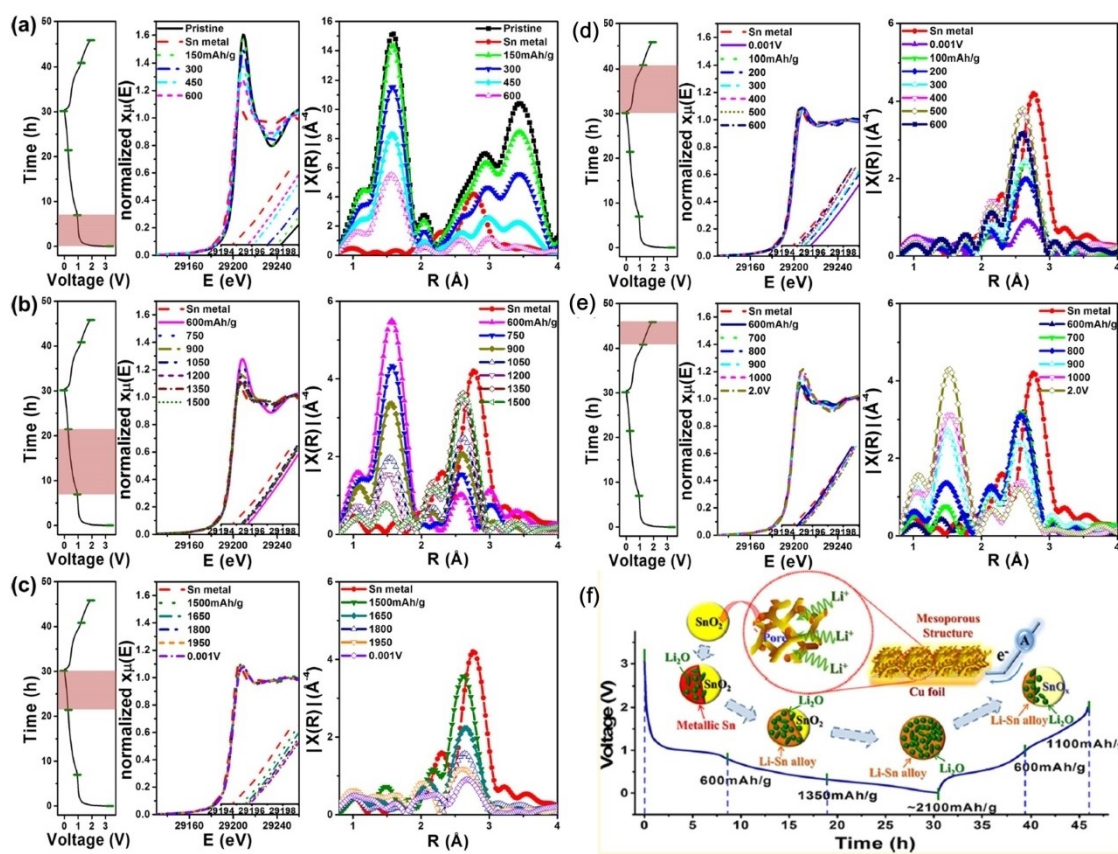
Figure 12. *In situ* Sn K-edge XANES and EXAFS spectra of mesoporous SnO_2 electrode with corresponding voltage profile taken in a) the first discharge region, b) the middle discharge region, c) the last discharge region, d) the first charge region, and e) the last charge region of first cycle. f) Schematic illustration of the electrochemical reaction mechanism of mesoporous SnO_2 during the initial cycle. Reproduced from Ref. [55] with permission. Copyright 2014, American Chemical Society.

Batteries & Supercaps

Review
doi.org/10.1002/batt.202100006

Chemistry
Europe
European Chemical
Societies Publishing

peak, indicating that the dealloying process of Li$_x$Sn phase and the conversion reaction of Sn into the SnO$_x$ phase occurs in this potential region. The EXAFS and diffraction results for the first discharging/charging cycle demonstrate that the pristine SnO$_2$ electrode does not recover to its initial composition but turns into metallic Sn, Li$_x$Sn, and amorphous SnO$_x$ after one complete cycle, which gives rise to exceptional high capacity for the ordered mesoporous SnO$_2$ electrode material.

In addition, Lowe et al.[56] used *operando* synchrotron XRD and XAS to study the conversion reaction mechanism of Mn$_3$O$_4$ for lithium-ion storage (Figure 13). The *operando* XRD results identified the reduction of Mn element and the generation of LiMn$_3$O$_4$ at the start of phase I and the generation of MnO after 0.5 e$^-$/Mn$_3$O$_4$. *Operando* XAS spectra during phase I show that the XANES edge continually shifts towards lower energies, suggesting gradual reduction of Mn in the electrode, whilst the decreasing pre-edge intensity suggests the transformation of the Mn coordination environment from tetrahedral to octahedral. During phase II and III, the isosbestic points of the XANES spectra reveal a two-phase conversion reaction between MnO and Mn. Meanwhile, the pre-edge feature downshifts in energy and increases in intensity, which suggests a reduction process

from MnO to metallic Mn with enhanced s-p hybridization of metallic bonding. FTs of the *operando* Mn K-edge EXAFS spectra of the electrode during phases II and III show consistent changes in the local coordination environment. The coordination number of the Mn—O shell and the Mn—Mn shell for MnO decreases gradually, whilst the Mn—Mn shell from metallic Mn becomes prominent. In summary, the conversion reaction mechanism in Mn$_3$O$_4$ electrode during lithiation follows the reaction sequence of Mn$_3$O$_4$→LiMn$_3$O$_4$→MnO→Mn. It is worth mentioning that Yun et al.[61] conducted in situ synchrotron XAS experiments to study the charge/discharge process of Fe$_3$O$_4$ for LIBs. By monitoring the reaction pathway and phase evolution of the Fe$_3$O$_4$/rGO composite, small domain size and highly disordered nature of Fe$_x$O$_y$ were identified. They ascribed the excellent electrode performance to the good contact between the pulverized Fe$_x$O$_y$ particles and rGO, the structural integrity, and the interconnected pores.

Sn$_4$P$_3$ has high initial capacities as a conversion-type anode for LIBs but shows rapid fading after tens of cycles. It converts to metallic Sn and Li$_3$P through a conversion reaction, followed by an alloying reaction between Sn and Li to form Li$_{22}$Sn$_5$. XRD studies of the Sn$_4$P$_3$ electrode show that crystalline Sn$_4$P$_3$
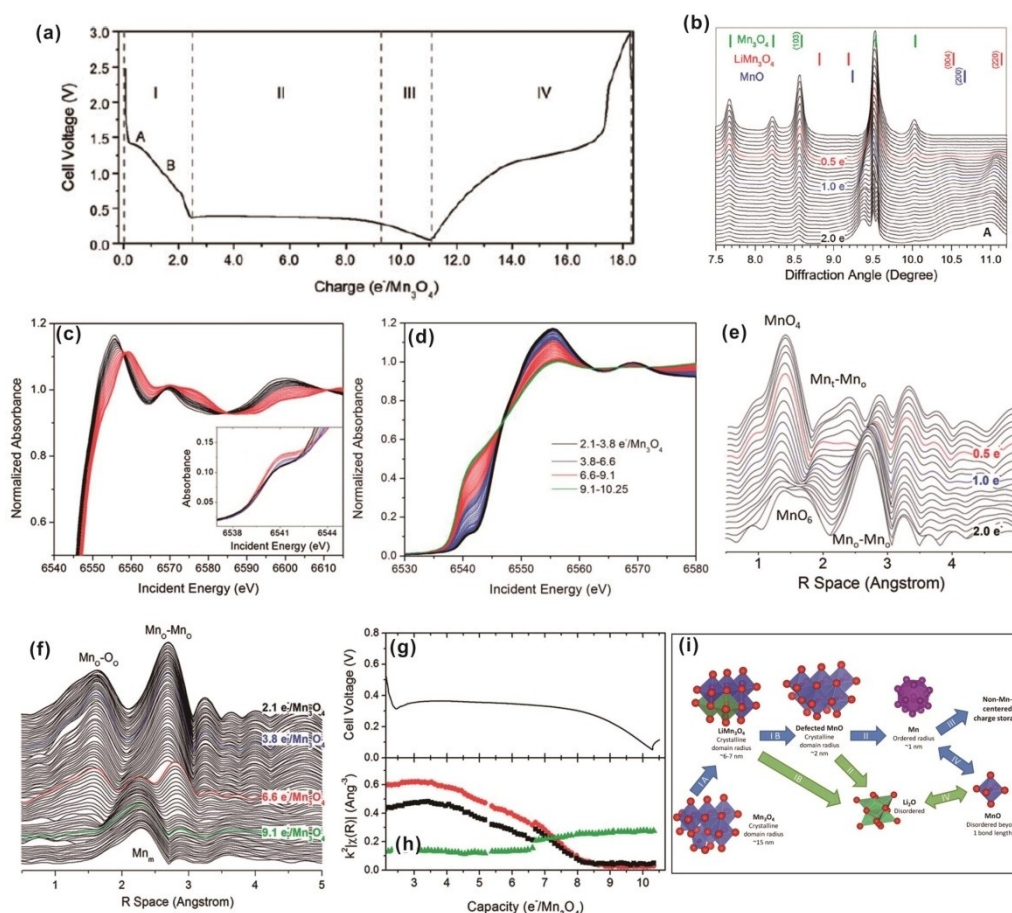
Figure 13. a) Discharging-charging profiles of Mn$_3$O$_4$ anodes in LIBs for the initial cycle. b) Operando XRD patterns during phase I, and operando Mn K-edge XANES spectra c) during phase I and d) phases II and III. The inset in c shows the corresponding pre-edge features. Red and black lines were recorded during the charge intervals 0.0–1.0 and 1.0–2.0 e$^-$/Mn$_3$O$_4$, respectively. FTs of operando Mn K-edge EXAFS spectra e) during phase I and f) phases II and III. g) Voltage profile and h) EXAFS intensity for peaks at 1.5 Å (black, octahedral Mn—O), 2.7 Å (red, Mn—Mn in MnO), and 2.3 Å (green, Mn—Mn in Mn metal). i) Proposed conversion reaction mechanism of Mn$_3$O$_4$ for LIBs. Reproduced from Ref. [56] with permission. Copyright 2013, The Royal Society of Chemistry.

Batteries & Supercaps

Review
doi.org/10.1002/batt.202100006

Chemistry
Europe
European Chemical
Societies Publishing

becomes amorphous with the absence of long-range order in the course of repeated cycling, which poses a challenge to further understanding of the fading mechanism.[83] Ding et al.[57] used *in situ* XAS to probe the local atomic structure changes of Sn_4P_3 anodes during repeated lithiation/delithiation processes. In the first two cycles, the Sn_4P_3 anode is not fully lithiated/ delithiated, with only minor changes of the coordination environment around Sn, and the authors ascribed this phenomenon to the lower pressure and unsatisfactory electrical conductivity in the window area of the *in situ* cell which caused incomplete reaction of Sn_4P_3. The coordination distance and coordination number in regards to Sn–Sn, Sn–O, Sn–P, and Sn–Li were compared for the first four cycles of the *in situ* cell and the 100th cycle of the *ex situ* cell at different charge states. It is concluded that the amorphous SnP_x phases formed during the initial two cycles showed high reversibility in the first several cycles whilst the gradual capacity fading could be attributed to the increasing size and amount of metallic Sn clusters in the delithiated state during long-term cycling, accompanying with a decreasing amount of amorphous SnP_x phases.

Besides, MoS_2, as one of the outstanding anodes for LIBs, were studied by Mo K-edge and S K-edge XAS measurement. However, the proposed conversion reaction mechanism of MoS_2 seems like controversial. Zhang et al.,[59] reported that the conversion reaction of MoS_2 is not reversible, where the formed Li_2S is converted to sulfur at the end of the initial charge and Li_2S/sulfur becomes the main redox couple in the subsequent cycles. Nevertheless, Zhu et al.[84] suggested that amorphous MoS_2 nanograins rather than sulfur are generated at the end of the initial charge, and the completely lithiated MoS_2 electrode consists of Mo, Li_2S, and additional unknown Mo–S related phases. Therefore, clarifying the detailed operating mechanism is important to design better MoS_2 electrode since it determines that the first choice is whether to buffer the large volume changes or to suppress the possible shuttle effect of polysulfides. Moreover, the SnS_2 anode for SIBs was studied by *in situ* Sn K-edge EXAFS experiments, revealing the formation of Na–Sn alloy phases during discharge.[58] Bi_2O_2Se was investigated as advanced anodes for lithium-ion batteries and potassium-ion batteries, and the mechanism were studied by *in situ* Bi L_{III}-edge and Se K-edge XAS. revealing an insertion-conversion-alloying process upon lithiation and the dissolution of Li–Se intermediate phases in the electrolyte.[67]

3.4. Beyond In Situ XAS Studies of Anodes

Beyond *in situ* measurements, XAS has also been used to study the electronic and local atomic structure of powder materials, electrolytes, and *cathode*s for battery application.

By comparing the local atomic information for different CoO electrode materials extracted from both the Co K-edge and O K-edge XAS spectra, the authors found that the anomalous capacity in nanosized (~7 nm) CoO can be associated with the formation of oxygen-rich CoO material.[85] By analyzing the neighboring environment around Mo atoms

in MoSSe, the authors demonstrated that high-concentration anion vacancies in MoSSe electrode facilitate fast and stable potassium ion storage.[86] Besides, Zhang et al.[87] developed potassium niobates as high-performance anodes for Li/K-ion storage, and Nb K-edge XAS spectra were measured to identify the valence states of Nb and to compare the ratio of oxygen vacancies in different potassium niobate samples.

Moreover, the solvation structure of the electrolyte ($LiBF_4$ in propylene carbonate) was studied by O K-edge soft XAS, revealing a Li^+-solvent interaction number of 4.5 by a linear combination of the spectra of Li^+-associating and free propylene carbonate molecules.[88] Solid electrolyte interphase (SEI) layers on the electrode/electrolyte interface were also studied by surface-sensitive soft XAS.[89] Last but not the least, synchrotron XAS was also widely used to characterize battery cathodes, which has been summarized in other reviews in detail.[25a,43,90] It is noted that cathode materials generally involves 3d transition metal elements, such as Fe, Co, Ni and Mn, whilst anode materials are related with more broad elemental families, including Si, Sn, Sb, Bi, Ti, Nb, Mo, etc., so the photon energy ranges are different for cathodes and anodes during XAS measurements, resulting with different sample preparation and experimental setup.

4. Summary and Outlook

In summary, synchrotron XAS is one of the state-of-the-art characterization techniques for studying the electrochemical reaction mechanisms of rechargeable batteries, which can provide abundant electronic and local atomic structure information on targeted elements of electrode materials. It shows unique advantages in detecting dynamic variations of local symmetry, charge transfer, oxidation state and local atomic structure of electrode materials during battery operation. By virtue of high-flux synchrotron light sources, researchers are able to conduct *in situ*, element-selective, and qualitative/ quantitative experiments at the XAS beamline end station efficiently and accurately. *In situ* XAS experiments can provide real-time spectroscopic information of an operating customized coin-cell, while element-selective experiments enables us to measure multi-elements for one electrode, which is advantageous to provide complementary and verifiable information for one electrode, while qualitative/quantitative analysis methods facilitates to provide informative results to interpret electrochemical reaction mechanisms of rechargeable batteries. By using *in situ* XAS to study insertion-type anode materials, abundant information can be extracted, including electron (and Li^+) transfer rates, oxidation state variations, local geometry evolutions, local symmetry distortions, and bond distortions. Regarding alloying-type anode materials, charge transfer processes and local atomic structure of intermediate phases (including possible amorphous phases and poor-crystalline phases in particular) can be revealed accordingly. In comparison with alloy-type anodes, additional redox reactions can be monitored by *in situ* XAS in conversion-type anodes. It is noted that synchrotron XAS is particularly suitable to identify the

Batteries & Supercaps

Review
doi.org/10.1002/batt.202100006

Chemistry Europe
European Chemical
Societies Publishing

amorphous phases and low-concentration components involved in the electrochemical reaction process. The advanced understanding of the structure-performance relationship of electrode materials will, in turn, inform enhanced battery design strategies.

Despite significant advances being made on the preparation and *in situ* measurement of anode materials over the past few years, there are still challenges to understand their complex electrochemical storage behaviors and propose feasible solutions that can make significant breakthroughs. *In situ* electrochemical experiments based on synchrotron XAS can provide a unique insight into the electrochemical reaction mechanisms for rechargeable batteries on high-resolution time scales and length scales, but there are also challenges, including

(i) in situ cells may suffer from nonequilibrium under large current density or high-mass loading, which may affect the understanding of *in situ* XAS spectra;

(ii) in situ cells may occasionally not operate identical to traditional (unmodified) cells due to poor contact below the holes and possible side reactions caused by the applied windows;

(iii) additional and/or unusual phenomena can be hidden as XAS measures the average local atomic information of a selected element;

(iv) in situ soft XAS experiments, especially targeted at light element such as O and N, are challenging due to the required high vacuum environment and can be impacted by electrolytes and substrates;

(v) the difficulties in data analysis and fitting pose a challenge to extract fruitful results from XAS;

(vi) applying for synchrotron XAS beamtime is highly competitive, and beamtime is limited, which suppresses the development of *in situ* XAS studies.

Most of *in situ* XAS studies mainly focus on Li-ion storage system, and it means that tremendous opportunities are presented for *in situ* XAS studies of Na-, K-, Zn-, Mg-ion batteries, where new energy storage mechanisms can be discovered. It is also expected that a more comprehensive understanding of the electrochemical reaction mechanisms can be obtained by combining several *in situ* advanced characterizations together. With the rapid development of synchrotron light sources, we believe the shortage of XAS beamtime will alleviate in the future and also provides an exciting opportunity to unravel unprecedented detail based on updated synchrotron light sources. For example, new medium energy beamlines (MEX1 & MEX2) are being commissioned at the Australian Synchrotron, Australia, while the High Energy Photon Source (HEPS), a 6 GeV green-field diffraction-limited storage ring light source, is being built in Beijing, China. Based on rational *in situ* cell design and comprehensive *in situ* multi-edge XAS measurements, future research based on XAS studies of battery materials will blossom by using this state-of-the-art characterization technique.

Conflict of Interest

The authors declare no conflict of interest.

Keywords: in situ · X-ray absorption spectroscopy · batteries · mechanism · anode materials

[1] D. Larcher, J.-M. Tarascon, *Nat. Chem.* **2015**, *7*, 19.

[2] J.-M. Tarascon, *Nat. Chem.* **2010**, *2*, 510–510.

[3] a) W. Zhang, Y. Liu, Z. Guo, *Sci. Adv.* **2019**, *5*, eaav7412; b) Z. Wu, G. Liang, W. K. Pang, T. Zhou, Z. Cheng, W. Zhang, Y. Liu, B. Johannessen, Z. Guo, *Adv. Mater.* **2020**, *32*, 1905632; c) H. Hou, C. E. Banks, M. Jing, Y. Zhang, X. Ji, *Adv. Mater.* **2015**, *27*, 7861–7866.

[4] a) P. Simon, Y. Gogotsi, B. Dunn, *Science* **2014**, *343*, 1210–1211; b) J. B. Goodenough, *Acc. Chem. Res.* **2013**, *46*, 1053–1061; c) J. B. Goodenough, *Nat. Electron.* **2018**, *1*, 204–204.

[5] J. Meng, H. Guo, C. Niu, Y. Zhao, L. Xu, Q. Li, L. Mai, *Joule* **2017**, *1*, 522–547.

[6] I. Sultana, T. Ramireddy, M. M. Rahman, Y. Chen, A. M. Glushenkov, *Chem. Commun.* **2016**, *52*, 9279–9282.

[7] B. Wang, B. Luo, X. Li, L. Zhi, *Mater. Today* **2012**, *15*, 544–552.

[8] Z. Wu, B. Johannessen, W. Zhang, W. K. Pang, J. Mao, H. K. Liu, Z. Guo, *J. Mater. Chem. A* **2019**, *7*, 12842–12850.

[9] C. K. Chan, H. Peng, G. Liu, K. McIlwrath, X. F. Zhang, R. A. Huggins, Y. Cui, *Nat. Nanotechnol.* **2008**, *3*, 31.

[10] J. S. Chen, X. W. Lou, *Small* **2013**, *9*, 1877–1893.

[11] L. Wang, X. Bi, S. Yang, *Adv. Mater.* **2016**, *28*, 7672–7679.

[12] M. R. Palacin, *Chem. Soc. Rev.* **2009**, *38*, 2565–2575.

[13] a) G.-L. Xu, T. Ma, C.-J. Sun, C. Luo, L. Cheng, Y. Ren, S. M. Heald, C. Wang, L. Curtiss, J. Wen, *Nano Lett.* **2016**, *16*, 2663–2673; b) F. Sun, C. Yang, I. Manke, L. Chen, S. Dong, *Mater. Today* **2020**, *38*, 7–9; c) F. Sun, D. Zhou, X. He, M. Osenberg, K. Dong, L. Chen, S. Mei, A. Hilger, H. Markötter, Y. Lu, *ACS Energy Lett.* **2019**, *5*, 152–161.

[14] a) Y. Liu, Y. Zhu, Y. Cui, *Nat. Energy.* **2019**, *4*, 540–550; b) S. Hu, A. S. Pillai, G. Liang, W. K. Pang, H. Wang, Q. Li, Z. Guo, *Electrochemical Energy Reviews* **2019**, 1–35; c) M. Li, C. Wang, Z. Chen, K. Xu, J. Lu, *Chem. Rev.* **2020**; d) G. Zampardi, F. La Mantia, *Batteries & Supercaps* **2020**, *3*, 672–697.

[15] a) Q. Gu, J. A. Kimpton, H. E. Brand, Z. Wang, S. Chou, *Adv. Energy Mater.* **2017**, *7*, 1602831; b) X. H. Liu, Y. Liu, A. Kushima, S. Zhang, T. Zhu, J. Li, J. Y. Huang, *Adv. Energy Mater.* **2012**, *2*, 722–741.

[16] Y. Sun, Y. Ren, *Part. Part. Syst. Charact.* **2013**, *30*, 399–419.

[17] a) G. Aquilanti, M. Giorgetti, R. Dominko, L. Stievano, I. Arčon, N. Novello, L. Olivi, *J. Phys. D* **2017**, *50*, 074001; b) Y. Cui, A. Abouimrane, J. Lu, T. Bolin, Y. Ren, W. Weng, C. Sun, V. A. Maroni, S. M. Heald, K. Amine, *J. Am. Chem. Soc.* **2013**, *135*, 8047–8056.

[18] G. Liang, C. Didier, Z. Guo, W. K. Pang, V. K. Peterson, *Adv. Mater.* **2020**, *32*, 1904528.

[19] a) M. Chen, S. L. Chou, S. X. Dou, *Batteries & Supercaps* **2019**, *2*, 842–851; b) C. Li, F. Geng, B. Hu, B. Hu, *Mater. Today* **2020**, 100474; c) J. Wu, Z.-x. Shen, W. Yang, *Front. Chem.* **2020**, *8*, 816.

[20] W. Klysubun, P. Sombunchoo, W. Deenan, C. Kongmark, *J. Synchrotron Radiat.* **2012**, *19*, 930–936.

[21] a) W.-S. Yoon, K. Y. Chung, J. McBreen, D. A. Fischer, X.-Q. Yang, *J. Power Sources* **2007**, *174*, 1015–1020; b) J. W. Smith, R. J. Saykally, *Chem. Rev.* **2017**, *117*, 13909–13934.

[22] F. Lin, Y. Liu, X. Yu, L. Cheng, A. Singer, O. G. Shpyrko, H. L. Xin, N. Tamura, C. Tian, T.-C. Weng, *Chem. Rev.* **2017**, *117*, 13123–13186.

[23] a) S. Calvin, *XAFS for Everyone*, CRC press, **2013**; b) Z. Sun, Q. Liu, T. Yao, W. Yan, S. Wei, *Sci. China Mater.* **2015**, *58*, 313–341.

[24] J. Zhong, H. Zhang, X. Sun, S. t. Lee, *Synchrotron Radiation in Materials Science: Light Sources, Techniques, and Applications* **2018**, *1*, 275–319.

[25] a) Q. Li, R. Qiao, L. A. Wray, J. Chen, Z. Zhuo, Y. Chen, S. Yan, F. Pan, Z. Hussain, W. Yang, *J. Phys. D* **2016**, *49*, 413003; b) J. Lu, T. Wu, K. Amine, *Nat. Energy* **2017**, *2*, 1–13.

[26] S. Kelly, D. Hesterberg, B. Ravel, *Methods of Soil Analysis Part 5 – Mineralogical Methods* **2008**, *5*, 387–463.

[27] S.-H. Yu, X. Feng, N. Zhang, J. Seok, H. c. D. Abruña, *Acc. Chem. Res.* **2018**, *51*, 273–281.

[28] M. Giorgetti, *ISRN Materials Science* **2013**, *2013*.

[29] B. Ravel, M. Newville, *J. Synchrotron Radiat.* **2005**, *12*, 537–541.

[30] B. Ravel, M. Newville, *Phys. Scr.* **2005**, *2005*, 1007.

[31] M. Fehse, A. Iadecola, M. T. Sougrati, P. Conti, M. Giorgetti, L. Stievano, *Energy Storage Mater.* **2019**, *18*, 328–337.

[32] C. Glover, J. McKinlay, M. Clift, B. Barg, J. Boldeman, M. Ridgway, G. Foran, R. Garret, P. Lay, A. Broadbent, in *AIP Conf. Proc., Vol. 882*, American Institute of Physics, **2007**, pp. 884–886.

[33] a) M. Giorgetti, L. Stievano, *X-ray Characterization of Nanostructured Energy Materials by Synchrotron Radiation* **2017**, 51–75; b) J. Zhong, H. Zhang, X. Sun, S. T. Lee, *Adv. Mater.* **2014**, *26*, 7786–7806.

[34] C. Bissardon, O. Proux, S. Bureau, E. Suess, L. H. Winkel, R. Conlan, L. W. Francis, I. Khan, L. Charlet, J.-L. Hazemann, *Analyst* **2019**, *144*, 3488–3493.

[35] K. Feng, H. Zhang, J. Gao, J. Xu, Y. Dong, Z. Kang, J. Zhong, *Appl. Phys. Lett.* **2020**, *116*, 191903.

[36] G. N. George, I. J. Pickering, M. J. Pushie, K. Nienaber, M. J. Hackett, I. Ascone, B. Hedman, K. O. Hodgson, J. B. Aitken, A. Levina, *J. Synchrotron Radiat.* **2012**, *19*, 875–886.

[37] G. Liang, Z. Wu, C. Didier, W. Zhang, J. Cuan, B. Li, K. Y. Ko, P. Y. Hung, C. Z. Lu, Y. Chen, *Angew. Chem. Int. Ed.* **2020**.

[38] D. Göries, B. Dicke, P. Roedig, N. Stübe, J. Meyer, A. Galler, W. Gawelda, A. Britz, P. Geßler, H. Sotoudi Namin, *Rev. Sci. Instrum.* **2016**, *87*, 053116.

[39] F. B. C. T. Chantler, B. Bunker, *International Tables for Crystallography Volume I: X-ray Absorption Spectroscopy and Related Techniques* **2020**, https://doi.org/10.1107/97809553602060000116.

[40] G. Liang, J. Hao, A. M. D'Angelo, V. K. Peterson, Z. Guo, W. K. Pang, *Batteries & Supercaps* **2021**, *4*, 380–384.

[41] T. G. Mayerhöfer, S. Pahlow, J. Popp, *ChemPhysChem* **2020**, *21*, 2029.

[42] D. Liu, Z. Shadike, R. Lin, K. Qian, H. Li, K. Li, S. Wang, Q. Yu, M. Liu, S. Ganapathy, *Adv. Mater.* **2019**, *31*, 1806620.

[43] a) M. Chen, S. Chou, S.-X. Dou, *Batteries & Supercaps* **2019**, *2*, 842–851; b) C. T. Love, A. Korovina, C. J. Patridge, K. E. Swider-Lyons, M. E. Twigg, D. E. Ramaker, *J. Electrochem. Soc.* **2013**, *160*, A3153.

[44] R. Kodama, Y. Terada, I. Nakai, S. Komaba, N. Kumagai, *J. Electrochem. Soc.* **2006**, *153*, A583–A588.

[45] K. J. Griffith, K. M. Wiaderek, G. Cibin, L. E. Marbella, C. P. Grey, *Nature* **2018**, *559*, 556–563.

[46] W. Zhang, M. Topsakal, C. Cama, C. J. Pelliccione, H. Zhao, S. Ehrlich, L. Wu, Y. Zhu, A. I. Frenkel, K. J. Takeuchi, *J. Am. Chem. Soc.* **2017**, *139*, 16591–16603.

[47] Y. Tang, Y. Zhang, O. I. Malyi, N. Bucher, H. Xia, S. Xi, Z. Zhu, Z. Lv, W. Li, J. Wei, *Adv. Mater.* **2018**, *30*, 1802200.

[48] A. Siebert, X. Dou, R. Garcia-Diez, D. Buchholz, R. Félix, E. Handick, G. Greco, I. Hasa, R. G. Wilks, S. Passerini, *ACS Appl. Energ. Mater.* **2021**, *4*, 164–175.

[49] C. J. Pelliccione, E. V. Timofeeva, C. U. Segre, *J. Phys. Chem. C* **2016**, *120*, 5331–5339.

[50] A. Darwiche, M. Fehse, A. Mahmoud, C. La Fontaine, B. Fraisse, R. P. Hermann, M.-L. Doublet, L. Monconduit, M. T. Sougrati, M. Ben Yahia, *Batteries* **2018**, *4*, 25.

[51] L. Y. Lim, N. Liu, Y. Cui, M. F. Toney, *Chem. Mater.* **2014**, *26*, 3739–3746.

[52] M. Fehse, M. T. Sougrati, A. Darwiche, V. Gabaudan, C. La Fontaine, L. Monconduit, L. Stievano, *J. Mater. Chem. A* **2018**, *6*, 8724–8734.

[53] A. Darwiche, F. Murgia, M. Fehse, A. Mahmoud, A. Iadecola, S. Belin, C. La Fontaine, V. Briois, R. P. Hermann, B. Fraisse, *Energy Storage Mater.* **2019**, *21*, 1–13.

[54] M. Fehse, A. Darwiche, M. T. Sougrati, E. M. Kelder, A. V. Chadwick, M. Alfredsson, L. Monconduit, L. Stievano, *Chem. Mater.* **2017**, *29*, 10446–10454.

[55] H. Kim, G. O. Park, Y. Kim, S. Muhammad, J. Yoo, M. Balasubramanian, Y.-H. Cho, M.-G. Kim, B. Lee, K. Kang, *Chem. Mater.* **2014**, *26*, 6361–6370.

[56] M. A. Lowe, J. Gao, H. D. Abruña, *J. Mater. Chem. A* **2013**, *1*, 2094–2103.

[57] Y. Ding, Z. F. Li, E. V. Timofeeva, C. U. Segre, *Adv. Energy Mater.* **2018**, *8*, 1702134.

[58] C. Ma, J. Xu, J. Alvarado, B. Qu, J. Somerville, J. Y. Lee, Y. S. Meng, *Chem. Mater.* **2015**, *27*, 5633–5640.

[59] L. Zhang, D. Sun, J. Kang, J. Feng, H. A. Bechtel, L.-W. Wang, E. J. Cairns, J. Guo, *Nano Lett.* **2018**, *18*, 1466–1475.

[60] T. Li, C. Lim, Y. Cui, X. Zhou, H. Kang, B. Yan, M. L. Meyerson, J. A. Weeks, Q. Liu, F. Guo, *J. Mater. Chem. A* **2020**, *8*, 750–759.

[61] S. Yun, S. M. Bak, S. Kim, J. S. Yeon, M. G. Kim, X. Q. Yang, P. V. Braun, H. S. Park, *Adv. Energy Mater.* **2019**, *9*, 1802816.

[62] F. Tavani, M. Fracchia, N. Pianta, P. Ghigna, E. Quartarone, P. D'Angelo, *Chem. Phys. Lett.* **2020**, *760*, 137968.

[63] T.-Y. Chen, S.-Y. Wang, C.-H. Kuo, S.-C. Huang, M.-H. Lin, C.-H. Li, H.-Y. T. Chen, C.-C. Wang, Y.-F. Liao, C.-C. Lin, *J. Mater. Chem. A* **2020**, *8*, 21756–21770.

[64] C.-C. Lin, C.-T. Hsu, W. Liu, S.-C. Huang, M.-H. Lin, U. Kortz, A. S. Mougharbel, T.-Y. Chen, C.-W. Hu, J.-F. Lee, *ACS Appl. Mater. Interfaces* **2020**, *12*, 40296–40309.

[65] M. R. Panda, R. Gangwar, D. Muthuraj, S. Sau, D. Pandey, A. Banerjee, A. Chakrabarti, A. Sagdeo, M. Weyland, M. Majumder, *Small* **2020**, *16*, 2002669.

[66] C. Li, A. Sarapulova, K. Pfeifer, X. Luo, N. P. Maria Casati, E. Welter, G. Melinte, Q. Fu, S. Dsoke, *ACS Appl. Mater. Interfaces* **2020**, *12*, 52691–52700.

[67] Z. Wu, G. Liang, J. Wu, W. K. Pang, F. Yang, L. Chen, B. Johannessen, Z. Guo, *Adv. Energy Mater.* **2021**, 2100185.

[68] a) Z. Chen, I. Belharouak, Y. K. Sun, K. Amine, *Adv. Funct. Mater.* **2013**, *23*, 959–969; b) Q. Deng, Y. Fu, C. Zhu, Y. Yu, *Small* **2019**, *15*, 1804884.

[69] G.-N. Zhu, Y.-G. Wang, Y.-Y. Xia, *Energy Environ. Sci.* **2012**, *5*, 6652–6667.

[70] M. Fehse, A. Henry, A. Zitolo, B. Boury, N. Louvain, L. Stievano, *Applied Sciences* **2020**, *10*, 5547.

[71] K. E. Silberstein, M. A. Lowe, B. Richards, J. Gao, T. Hanrath, H. c. D. Abruña, *Langmuir* **2015**, *31*, 2028–2035.

[72] L. Baggetto, K. J. Carroll, H.-Y. Hah, C. E. Johnson, D. R. Mullins, R. R. Unocic, J. A. Johnson, Y. S. Meng, G. M. Veith, *J. Phys. Chem. C* **2014**, *118*, 7856–7864.

[73] I. Devos, M. Womes, M. Heilemann, J. Olivier-Fourcade, J.-C. Jumas, J. L. Tirado, *J. Mater. Chem.* **2004**, *14*, 1759–1767.

[74] C. Marino, C. Fraisse, M. Womes, C. Villevieille, L. Monconduit, L. Stievano, *J. Phys. Chem. C* **2014**, *118*, 27772–27780.

[75] S. Yoon, J.-M. Lee, H. Kim, D. Im, S.-G. Doo, H.-J. Sohn, *Electrochim. Acta* **2009**, *54*, 2699–2705.

[76] C. J. Pelliccione, Y. Ding, E. V. Timofeeva, C. U. Segre, *J. Electrochem. Soc.* **2015**, *162*, A1935–A1939.

[77] M. M. Huie, D. C. Bock, L. Wang, A. C. Marschilok, K. J. Takeuchi, E. S. Takeuchi, *J. Phys. Chem. C* **2018**, *122*, 10316–10326.

[78] Y. Zhou, H. Xie, C. Wang, Q. He, Q. Liu, Z. Muhammad, Y. A. Haleem, Y. Sang, S. Chen, L. Song, *J. Phys. Chem. C* **2017**, *121*, 15589–15596.

[79] A. V. Chadwick, S. L. Savin, S. Fiddy, R. Alcantara, D. Fernández Lisbona, P. Lavela, G. F. Ortiz, J. L. Tirado, *J. Phys. Chem. C* **2007**, *111*, 4636–4642.

[80] L. Peng, P. Xiong, L. Ma, Y. Yuan, Y. Zhu, D. Chen, X. Luo, J. Lu, K. Amine, G. Yu, *Nat. Commun.* **2017**, *8*, 1–10.

[81] D. Zhou, H. Jia, J. Rana, T. Placke, T. Scherb, R. Kloepsch, G. Schumacher, M. Winter, J. Banhart, *Electrochim. Acta* **2017**, *246*, 699–706.

[82] C. A. Cama, C. J. Pelliccione, A. B. Brady, J. Li, E. A. Stach, J. Wang, J. Wang, E. S. Takeuchi, K. J. Takeuchi, A. C. Marschilok, *Phys. Chem. Chem. Phys.* **2016**, *18*, 16930–16940.

[83] a) Y.-U. Kim, C. K. Lee, H.-J. Sohn, T. Kang, *J. Electrochem. Soc.* **2004**, *151*, A933–A937; b) B. León, J. I. Corredor, J. L. Tirado, C. Pérez-Vicente, *J. Electrochem. Soc.* **2006**, *153*, A1829–A1834.

[84] Z. Zhu, S. Xi, L. Miao, Y. Tang, Y. Zeng, H. Xia, Z. Lv, W. Zhang, X. Ge, H. Zhang, *Adv. Funct. Mater.* **2019**, *29*, 1904843.

[85] C. Chen, B. Hwang, J. Do, J. Weng, M. Venkateswarlu, M. Cheng, R. Santhanam, K. Ragavendran, J. Lee, J. Chen, *Electrochem. Commun.* **2010**, *12*, 496–498.

[86] H. He, D. Huang, Q. Gan, J. Hao, S. Liu, Z. Wu, W. K. Pang, B. Johannessen, Y. Tang, J.-L. Luo, *ACS Nano* **2019**, *13*, 11843–11852.

[87] S. Zhang, Q. Fan, Y. Liu, S. Xi, X. Liu, Z. Wu, J. Hao, W. K. Pang, T. Zhou, Z. Guo, *Adv. Mater.* **2020**, *32*, 2000380.

[88] J. W. Smith, R. K. Lam, A. T. Sheardy, O. Shih, A. M. Rizzuto, O. Borodin, S. J. Harris, D. Prendergast, R. J. Saykally, *Phys. Chem. Chem. Phys.* **2014**, *16*, 23568–23575.

[89] a) C. Yogi, D. Takamatsu, K. Yamanaka, H. Arai, Y. Uchimoto, K. Kojima, I. Watanabe, T. Ohta, Z. Ogumi, *J. Power Sources* **2014**, *248*, 994–999; b) A. Di Cicco, A. Giglia, R. Gunnella, S. L. Koch, F. Mueller, F. Nobili, M. Pasqualini, S. Passerini, R. Tossici, A. Witkowska, *Adv. Energy Mater.* **2015**, *5*, 1500642; c) R. Qiao, I. T. Lucas, A. Karim, J. Syzdek, X. Liu, W. Chen, K. Persson, R. Kostecki, W. Yang, *Adv. Mater. Interfaces* **2014**, *1*, 1300115.

[90] J. Lu, T. Wu, K. Amine, *Nat. Energy.* **2017**, *2*, 1–13.